

---

---

**BWX Technologies, Inc.**

**BWXT Services, Inc.**

**FINAL REPORT:**  
**EXAMINATION OF THE REACTOR VESSEL (RV) HEAD DEGRADATION  
AT DAVIS-BESSE**

**PREPARED FOR  
FRAMATOME ANP, INC.**

BWXT Services, Inc. makes no warranty or representation, expressed or implied:

- relative to the accuracy, completeness, or usefulness of the information contained in this report;
- or that the use of any information, apparatus, method, or process disclosed in this report may not infringe privately owned rights.

BWXT Services, Inc. assumes no liability with respect to the use of, or for damages resulting from the use of:

- any information, apparatus, method, or process disclosed in this report;
- or any experimental apparatus furnished with this report.

**BWXT SERVICES, INC.**

a McDermott company

Nuclear & Environmental Operations

---

**FINAL REPORT:**

**EXAMINATION OF THE REACTOR VESSEL (RV) HEAD DEGRADATION  
AT DAVIS-BESSE**

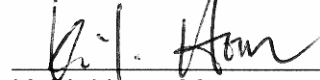
PREPARED BY:

BWXT SERVICES, INC.  
2016 MOUNT ATHOS ROAD  
LYNCHBURG, VIRGINIA 24504-5447  
(434) 522-6000

PREPARED BY:

  
\_\_\_\_\_  
J. W. Hyres, P. E., Principal Engineer  
Nuclear Materials Engineering

APPROVED BY:

  
\_\_\_\_\_  
K. Y. Hour, Manager  
Nuclear Materials Engineering

## SUMMARY

A portion of the degraded reactor vessel (RV) head and two control rod drive mechanism (CRDM) nozzles removed from Davis-Besse were submitted to the BWXT Services, Inc. Lynchburg Technology Center for metallurgical examinations. The primary objective of these examinations was to characterize the as-found condition of the head, which contained a large cavity caused by boric acid corrosion and examine the nozzles for evidence of cracking. Examinations included visual inspections, dye penetrant testing, scanning electron microscopy (SEM), energy dispersive spectroscopy (EDS), metallography, and Knoop microhardness.

The axial crack found on the uphill side of Alloy 600 CRDM nozzle #3 was typical of primary water stress-corrosion cracking (PWSCC). This cracking initiated on the nozzle I.D. surface and propagated in an intergranular fashion. The large grain size (ASTM 3) and the discontinuous intergranular carbides observed in this heat of material contributed to its PWSCC susceptibility.

The axial cracks found in the nozzle #3 J-groove weld on both the uphill and downhill sides were also typical of PWSCC in Alloy 182 and Alloy 82 weld metal alloys. Cracking in these areas progressed in an interdendritic or intergranular fashion. Cracking was more pronounced on the downhill side, which corresponded to the large corrosion cavity location. The wider opening observed on the axial crack on the downhill was likely due to the flow of primary coolant leaking through the crack. There was no conclusive evidence that hot cracking contributed to the J-groove weld cracking.

The exposed Type 308 stainless steel cladding surface area was approximately 16.5 square inches. The average cladding thickness measured by dial calipers was 0.256", with a minimum thickness of 0.202" and maximum thickness of 0.314". Thickness measurements taken on a transverse metallographic mount prepared through the thinnest portion of exposed cladding indicated a minimum cladding thickness of 0.179". This area, which was located in an uncracked region of the cladding adjacent to the J-groove weld, was not accessible during the dial caliper measurements. The cladding mechanical properties and chemical composition appeared uniform across the cladding thickness. The underside (reactor coolant system or RCS side) of the cladding and the unexposed portions of cladding did not contain any cracks or other signs of deterioration.

Shallow intergranular attack (IGA) was observed on all exposed cladding surfaces examined. Deeper cracks, which extended a maximum 0.057" below the exposed cladding surface, followed a mixed interdendritic/intergranular path. These cracks initiated in the IGA and propagated under a stress-corrosion cracking mechanism along the ferrite stringers under the influence of an applied tensile stress (i.e., system pressure). The minimum observed distance from an exposed cladding crack tip to the RCS side of the cladding was 0.188".

## **SUMMARY (CONTINUED)**

The striations on the cavity side wall (low alloy steel) appear to be influenced by the boric acid solution level in the cavity initially and the RV head microstructure afterward. The banded microstructure of the low alloy steel plate showed good correlation with the preferential corrosion that produced the striated texture. There was no evidence of erosion present on the as-found cavity walls; however, erosion may have played a part in the initial cavity formation.

The undercut regions observed in the low alloy steel around the perimeter of the exposed cladding were due to localized galvanic corrosion between the low alloy steel and the stainless steel. There was no evidence of cracking or disbond between the low alloy steel and stainless steel cladding in the undercut regions or outside the cavity.

## TABLE OF CONTENTS

<u>SECTION</u>	<u>PAGE</u>
1.0 INTRODUCTION.....	1
1.1 Background.....	1
1.2 Materials and Fabrication.....	1
2.0 CRDM NOZZLE INSPECTIONS.....	2
2.1 Nozzle #2 Visual Inspections.....	2
2.2 Nozzle #3 Visual Inspections.....	2
2.3 Nozzle #3 Initial Sectioning.....	3
2.4 Nozzle #3 Penetrant Testing.....	3
2.5 Nozzle #3 Additional Sectioning for Metallography and SEM/EDS.....	3
2.6 Nozzle #3 Metallography/Microhardness.....	4
2.7 Nozzle #3 SEM/EDS Examinations.....	4
3.0 CAVITY AND J-GROOVE WELD NON-DESTRUCTIVE TESTING.....	5
3.1 Receipt Inspections.....	5
3.2 Dental Molds.....	6
3.3 Initial Sectioning of Cavity.....	6
3.4 Fluorescent Penetrant Inspections.....	6
3.5 Area of Exposed Cladding and Cladding Thickness Measurements.....	7
3.6 Additional Visual Inspections.....	7
4.0 NON-EXPOSED CLADDING AND LOW ALLOY STEEL TESTING.....	9
4.1 Sectioning of Block "B".....	9
4.2 Metallography/Microhardness.....	9
4.3 Tensile Testing of Cladding.....	10
5.0 SECTIONING OF CAVITY.....	10
6.0 EXPOSED CLADDING TESTING.....	11
6.1 Near Center Crack (Sample A2A7M).....	11
6.1.1 Metallography/Microhardness.....	11
6.1.2 SEM/EDS.....	12
6.2 ~1/2" from Center Crack toward 270° (Sample A2A7N).....	12
6.2.1 Metallography.....	12
6.2.2 SEM/EDS.....	12
6.3 ~3/4" from Center Crack toward 90° (Sample A2A7S).....	13
6.3.1 Metallography/Microhardness.....	13
6.3.2 SEM/EDS.....	13
6.4 Main Crack Opened Up (Sample A2A7L).....	13
6.4.1 SEM/EDS.....	13
6.5 Mounted Sample through Thin Area of Cladding near 90° (Sample A2A5C).....	14
6.5.1 Metallography/Microhardness.....	14

## TABLE OF CONTENTS (CONTINUED)

<u>SECTION</u>	<u>PAGE</u>
7.0	NOZZLE #3 J-GROOVE WELD TESTING..... 14
7.1	Axial Crack near 180° ..... 15
7.1.1	Metallography/Microhardness ..... 15
7.2	Axial Crack near ~10° ..... 15
7.2.1	Metallography of Upper Portion of Crack..... 15
7.2.2	SEM/EDS of Upper Portion of Crack (Mounted Sample)..... 16
7.2.3	Metallography of Lower Portion of Crack..... 16
7.2.4	SEM/EDS of Middle Portion of Crack (Open Crack Sample)..... 16
7.3	Circumferential Cracking from ~0° to ~45° on RCS Side ..... 17
7.3.1	Metallography near 45° ..... 17
7.3.2	Metallography near 20° ..... 17
7.3.3	SEM/EDS near 20° (Mounted Sample) ..... 18
7.3.4	SEM/EDS near 30° (Open Crack Sample) ..... 18
8.0	CAVITY WALL AND UNDERCUT REGIONS..... 19
8.1	Cavity Wall Inspections near 90° ..... 19
8.1.1	Metallography of Upper Portion of Cavity Wall ..... 19
8.1.2	Metallography of Lower Portion of Cavity Wall ..... 19
8.1.3	SEM of Middle Portion of Cavity Wall ..... 19
8.2	Cavity Wall Inspections near 270° ..... 20
8.2.1	Macro Etch Test ..... 20
8.2.2	Metallography of Upper Portion of Cavity Wall ..... 20
8.2.3	Metallography of Lower Portion of Cavity Wall ..... 20
8.2.4	SEM of Middle Portion of Cavity Wall ..... 20
8.3	Examination of Undercut Regions ..... 20
8.3.1	Metallography near 345° ..... 20
8.3.2	Metallography near 10° (Nose of Cavity)..... 21
8.3.3	Metallography near 40° ..... 21
9.0	SUMMARY AND CONCLUSIONS ..... 22
10.0	REFERENCE ..... 23

## 1.0 INTRODUCTION

### 1.1 Background

Davis-Besse Nuclear Power Station in Oak Harbor, Ohio is a Babcock & Wilcox (B&W) designed 177-FA (fuel assembly) pressurized water reactor (PWR), which went into commercial operation in 1977. Davis-Besse initiated its 13th refueling outage (13RFO) in February 2002 after an accumulated 15.78 effective full power years (EFPYs) of operation. After removal of insulation from the reactor vessel (RV) head, boric acid crystal deposits and iron oxide were found to have flowed out from several of the openings in the lower service structure support skirt. Schematic diagrams showing the Davis-Besse RV head and the J-groove weld configuration are provided in Figure 1.1.1. Subsequent non-destructive examinations (NDE) identified axial cracks in five control rod drive mechanism (CRDM) nozzles adjacent to the J-groove weld. In three CRDM nozzles (#1, #2, and #3) located near the center of the RV head, the through-wall axial cracks extended above the J-groove weld. On-site NDE examinations detected 4 axial cracks in nozzle #3 near the J-groove weld as indicated in Figure 1.1.2. No NDE was performed to identify cracking in the CRDM nozzle J-groove weld.

Initially, it was decided that the five CRDM nozzles would be repaired by boring out the original J-groove weld and the lower part of the nozzle containing the cracks, and re-welding the remaining nozzle back to the RV head. Nozzle #3 was removed by boring from below to a height slightly above the J-groove weld on the uphill side (approximately 26.5 inches from the top of the CRDM flange). After boring out the lower part of nozzle #3, a large corrosion cavity was found on the downhill side of the low alloy steel RV head. Subsequently, a 17.5 inch diameter disc containing the remaining portion of the nozzle #3 J-groove weld, part of the nozzle #11 J-groove weld, and the entire cavity was sectioned from the RV head by water jet cutting. This disc along with the remnants of nozzles #2 and #3 were submitted to the BWXT Services, Inc. Lynchburg Technology Center for metallurgical examinations. The primary objective of these examinations was to characterize the condition of the RV head and examine the nozzles for evidence of cracking. Examinations included visual inspections, fluorescent dye penetrant testing, dimensional measurements, tensile testing, scanning electron microscopy (SEM), energy dispersive spectroscopy (EDS), metallography, and Knoop microhardness.

### 1.2 Materials and Fabrication

The CRDM nozzles were fabricated from Alloy 600 seamless tubing per ASME SB-167-1965<sup>1</sup>. CRDM nozzles #1 to #5 were fabricated from Heat M3935, which was supplied by the B&W Tubular Products Division (B&W TPD). Currently, there have been more leaking CRDM nozzles from Heat M3935 than from any other single heat used in the B&W 177-FA PWRs. The final mill anneal temperature is estimated to be 1600-1700°F. The chemical composition and mechanical properties from the certified material test report (CMTR) for Heat M3935 are listed in Table 1.2.1. The rough and final nozzle machining was performed after the final mill anneal. The final dimensions of the CRDM nozzles are approximately 4.00 inches outer diameter (OD) with a 0.625 inch wall thickness.

Table 1.2.1: CRDM Nozzle #3, Heat M3935 CMTR data.

C	Mn	Fe	S	Si	P	Cu	Ni	Cr	Co
0.028	0.27	6.25	0.0022	0.37	0.0040	0.01	77.89	15.58	0.010
Yield Strength				Tensile Strength				Elongation	
48.5 ksi (334 MPa)				85.6 ksi (590 MPa)				60%	

The CRDM penetrations were machined in the SA-533 Gr. B (mod) Cl. 1 RV head, which was previously clad with Type 308 stainless steel (see Figure 1.1.1). This cladding was applied to the reactor coolant system (RCS) side of the reactor vessel head as a corrosion barrier. The minimum specified thickness of this layer is 0.125 inch with a nominal thickness of  $\sim 3/16$  inch. The cladding was applied using an automated six-wire process, beginning near the edge of the vessel head and working toward the center in a circular pattern. The final  $\sim 8$ " diameter of the vessel head near the top dead center (TDC) was clad using a manual single-wire process.

The CRDM J-groove weld preparations were then ground into the RV head. After grinding, the J-groove weld preparations were buttered with Alloy 182 (E-NiCrFe-3) using the manual metal arc welding process. After the buttering operation, the RV head was stress relieved at  $1125 \pm 40^\circ\text{F}$  for 8 hours. Each Alloy 600 nozzle was custom ground for a diametrical interference fit of 0.0010 to 0.0021 inch with the CRDM penetrations in the RV head. Each nozzle was then attached to the RV head by a partial penetration weld (J-groove weld) using Alloy 182 filler material. No post weld stress relief was performed after J-groove welding. During plant operation, the temperature near the J-groove weld locations is estimated to be  $605^\circ\text{F}$ .

## 2.0 CRDM NOZZLE INSPECTIONS

### 2.1 Nozzle #2 Visual Inspections

Figure 2.1.1 provides a side view macro photograph showing the as-received condition of nozzle #2. The measured distance from the underside of the flange to the end of the nozzle was  $20\text{-}3/8$ " and the reduced diameter portion of the nozzle end measured  $3\text{-}3/8$ ". These measurements indicated approximately  $7\text{-}5/8$ " of the nozzle end was bored away during the nozzle removal process from the RV head. Figure 2.1.2 shows the end view of nozzle #2. It was determined that the boring tool extended approximately 3" up into the lower end of the nozzle. Visual inspections on the lower end of this nozzle revealed no evidence of cracking; it is believed that the cracks were bored out during the removal process.

### 2.2 Nozzle #3 Visual Inspections

An overall photograph showing the as-received condition of nozzle #3 is presented in Figure 2.2.1. The measured distance from the underside of the flange to the end of the nozzle was  $23\text{-}5/8$ " and the reduced diameter portion of the nozzle end measured  $6\text{-}1/2$ ". These measurements indicated approximately  $4\text{-}1/2$ " of the nozzle end was bored away

during the nozzle removal process. Higher magnification photographs showing the lower end of nozzle #3 are provided in Figure 2.2.2.

*Note: Rotational orientations to the in-service position of nozzle #3 are referenced in Figure 2.2.2. These orientations were established by assigning the 0° position to the plant southeast (i.e., nozzle #3 to nozzle #11 direction) and increasing degrees in the clockwise direction when looking at the top of the RV head. Using these orientations, the downhill side of nozzle #3 is located at 0° and the uphill side is at 180°. The head cavity was on the downhill side of nozzle #3 centered near the 10° position.*

These photographs show the bright appearance of the nozzle outer diameter (OD) that was adjacent to the corrosion cavity from approximately 270° - 0° - 90°. The bright appearance was due to the oxide film being removed by the boric acid in the corrosion cavity on the downhill side. The opposite side of the nozzle OD in contact with the RV head contained a fairly uniform dark oxide layer. Figure 2.2.3 shows the end view of nozzle #3. Unlike nozzle #2, the remaining portion of nozzle #3 had its full wall thickness on the lower end.

### 2.3 Nozzle #3 Initial Sectioning

Figure 2.3.1 provides the initial section locations for nozzle #3. Two transverse sections were made through the nozzle from the lower end as shown in Figure 2.3.1. These cuts were made using a lubricated horizontal band saw. The lowest piece (piece C) was a 1" wide ring potentially containing in-service cracks; the 2-1/2" ring was designated piece B and was shipped to Argonne National Laboratory for additional testing. The testing to be performed at Argonne National Laboratory is outside the scope of this investigation. No work was performed on the balance of the nozzle, which was designated piece A.

### 2.4 Nozzle #3 Penetrant Testing

A fluorescent dye penetrant test was performed on the exposed surfaces of piece C. This test revealed several axial cracks present on the lower portion of the nozzle inner diameter (ID) surface near the 180° orientation (i.e., uphill side of nozzle opposite the cavity). Refer to Figure 2.4.1 for the results of this examination. The largest crack in this area extended approximately 0.5" in length axially and ~0.125" deep radially from the ID surface of the nozzle. No other indications were found. It is evident that all other cracks identified by on-site NDE were within the 4-1/2" section bored away during the CRDM nozzle removal process.

### 2.5 Nozzle #3 Additional Sectioning for Metallography and SEM/EDS

Additional sectioning was required on the piece C ring to produce samples suitable for metallography and SEM/EDS. These sections were made using either electrical discharge machining (EDM) or a precision diamond cut-off saw. The details of sectioning along with the identifications of the newly created samples are provided in Figures 2.5.1 and 2.5.2. The primary objective of this sectioning was to separate the largest crack into three sections axially. This was accomplished by removing a ~1" wide by ~0.5" deep section containing the nozzle cracks. The piece containing the cracks was designated piece C1 and the remaining piece of the nozzle was designated piece C2 (spare). Piece C1 was then split twice in the transverse direction, creating pieces C1A (lowermost portion of

crack), C1B (central portion of crack), and C1C (uppermost portion of crack). To facilitate opening the lowermost portion of the crack for SEM/EDS, an additional section was made approximately parallel to and ~1/8" behind the nozzle ID surface. This cut produced pieces C1A1 (SEM/EDS sample) and C1A2 (spare).

The lowermost section was opened up for SEM/EDS analysis, the central portion was mounted for metallographic examinations (light microscopy and SEM/EDS), and the uppermost section is planned to be shipped to Pacific Northwest Laboratory (PNL) for additional laboratory analysis, which is outside the scope of this investigation.

## 2.6 Nozzle #3 Metallography/Microhardness

Nozzle #3 piece C1B was ground and polished for metallographic examinations using standard techniques. The samples were examined in the as-polished condition and after chemical etching to reveal the microstructure. For the nozzle sample, the dual etch technique (electrolytic phosphoric followed by electrolytic nital) was used. A series of Knoop microhardness readings (500 gram load) was also taken on this sample to characterize the base material hardness. These readings started near the nozzle ID surface and progressed toward the OD surface in ~0.050" increments.

Figure 2.6.1 provides a low magnification photograph of the mounted sample C1B. In this photograph, the largest crack is visible near 180° along with the string of Knoop microhardness indents near 175°. The base material hardness was generally uniform across the nozzle wall in the area tested and ranged from HK 179.1 to 221.3 (refer to the table in Figure 2.6.1).

Figure 2.6.2 provides higher magnification micrographs of the largest crack at 180°, which extended approximately 0.1" below the nozzle ID surface. The crack path is clearly intergranular in nature. The same crack morphology was observed for a smaller crack located near 170° (Figure 2.6.3). This crack extended approximately 0.05" below the nozzle ID surface. Micrographs showing the typical appearance of the nozzle base material microstructure are provided in Figure 2.6.4 (100X) and Figure 2.6.5 (375X). The microstructure consisted of equiaxed grains ranging in size from ASTM 1 to 6, with an average size of ASTM 3. Also observed throughout the microstructure were titanium or niobium carbonitrides (large yellow-to-orange color particles in Figure 2.6.6) and a semi-continuous to discontinuous network of grain boundary carbides.

## 2.7 Nozzle #3 SEM/EDS Examinations

High magnification SEM examinations were performed on the mounted sample and the opened crack sample. Both secondary electron (SE) and backscattered electron (BSE) imaging modes were utilized during this examination. SE imaging was employed to document the general topography of the fracture surfaces, while backscattered electron (BSE) imaging was utilized to identify chemical composition differences present in the microstructure and on the fracture surfaces. BSE image contrast varies with atomic number, with lighter atomic number regions appearing dark and higher atomic number regions appearing bright. The EDS attachment on the SEM was used to qualitatively identify the elemental constituents present at specific regions of interest within the

specimens. It was also used to semi-quantitatively determine the nozzle base metal chemical composition.

### *Mounted Sample*

The mounted sample discussed in Section 2.6 above was also examined by SEM/EDS. The sample was examined in the as-polished condition (i.e., no chemical etching). Low magnification micrographs of the largest crack are presented in both the SE and BSE imaging modes in Figure 2.7.1. The full crack length is shown in Figure 2.7.2. In this area, the crack extended approximately 0.08" below the nozzle ID surface. Cracking was also intergranular in nature. A higher magnification micrograph showing the typical grain boundary appearance is provided along with the EDS results in Figure 2.7.3. These results indicated the primary grain boundary constituents were carbon, oxygen, aluminum, nickel, chromium and iron. A very high magnification micrograph and corresponding EDS results are provided in Figure 2.7.4. For this area, the grain boundary composition (solid fill spectrum) is compared to the bulk grain composition (line spectrum). These results clearly show increased oxygen, chromium, and iron as well as diminished nickel at the grain boundary compared to the bulk grain chemical composition. Semi-quantitative EDS analysis was used to determine the nozzle base material chemical composition. These results, which are presented in Figure 2.7.5, were consistent with those expected for Alloy 600.

### *Open Crack Sample*

The lower portion of the largest crack was opened up for SEM/EDS examinations. Low magnification micrographs taken in the SE and BSE imaging modes are presented in Figures 2.7.6 and 2.7.7, respectively. The in-service cracking was intergranular and extended approximately 0.12" maximum below the nozzle ID surface. In the BSE imaging mode, the in-service fracture surface exhibited a darker contrast compared to the laboratory fracture, which is indicative of an oxide layer (i.e., lower atomic number) on the in-service fracture surface. SE micrographs showing the typical appearance of the fracture surface near the nozzle ID surface and toward the crack tip are provided in Figure 2.7.8. The intergranular grain facet selected for EDS analysis is shown in Figure 2.7.9 along with the EDS spectrum. In this area, the grain boundary layer contained carbon, oxygen, aluminum, silicon, chromium, iron, and nickel, along with a trace amount of titanium.

## 3.0 CAVITY AND J-GROOVE WELD NON-DESTRUCTIVE TESTING

### 3.1 Receipt Inspections

The as-received RV head section measured approximately 17" in diameter and 7" thick (Figures 3.1.1 and 3.1.2). This section contained the nozzle #3 bore, the corroded cavity, and a portion of the nozzle #11 bore. There was corrosion wastage on the top surface of the RV head in the areas adjacent to the cavity. In fact, it appeared that the only remaining original RV head surface present on this piece was located on the uphill side of the nozzle #3 bore at the 180° orientation (right side of Figure 3.1.3 and left side of Figure 3.1.4). Also evident in Figures 3.1.3 and 3.1.4 is the striated appearance of the cavity side wall. These striations were most prominent near the mid-thickness of the RV head. The striations diminish as the exposed surface of the stainless steel cladding is approached. Figure 3.1.5

is a view of the sample looking toward the uphill (180°) side of the nozzle #3 bore and Figure 3.1.6 shows the nose of the cavity near the 10° orientation. It was determined that the distance from the nozzle #3 bore to the nose of the cavity was approximately 6 inches.

### 3.2 Dental Molds

In order to capture a permanent replica of the cavity, two dental molds were made (the second mold served as a back-up). The mold set-up is shown in Figure 3.2.1. The mold compound was poured into the cavity and on the corroded portion of the RV head adjacent to the cavity. The completed dental mold is shown at four orthogonal orientations in Figure 3.2.2. In addition, a dental mold of the stainless steel cladding from the underside (RCS side) of the cavity was made to capture any plastic deformation to the cladding. A photograph of this mold is provided in Figure 3.2.3.

### 3.3 Initial Sectioning of Cavity

In order to reduce the size of the RV head section and isolate the cavity, several initial sections were required. These cuts were made using a cooled horizontal band saw. The first three cuts, which are shown schematically in Figure 3.3.1, created block A (containing cavity), B (toward 270°), C (toward 90°), and D (toward 0° and containing nozzle #11 bore). The fourth cut was made through block D parallel to and approximately 2 inches above the RCS side of the cladding (Figure 3.3.2). This created pieces D1 (upper) and D2 (lower). Piece D2 was shipped to Argonne National Laboratory for additional testing. The tests to be performed at Argonne National Laboratory are outside the scope of this investigation.

The fifth cut was made through the cavity in block A parallel to and approximately 2 inches above the exposed cladding surface (Figure 3.3.2). This cut, which created pieces A1 (upper) and A2 (lower), was made to facilitate the cladding thickness measurements and visual inspections.

### 3.4 Fluorescent Penetrant Inspections

Fluorescent dye penetrant tests were conducted on the cut surfaces of cuts #1, #2, and #3 to characterize the bondline between the stainless steel cladding and the RV head. No evidence of disbond was noted in any of the areas examined. A few small voids were noted in the nozzle #11 J-groove weld adjacent to the low alloy steel RV head on the cut #3 surface (Figure 3.4.1).

A penetrant test was also performed on the RCS side of the cladding below the cavity. The results, shown in Figure 3.4.2, indicated no evidence of cracking in the deflected region below the cavity. A discontinuous string of short circumferential indications was observed on the nozzle #3 J-groove weld surface approximately 0.75" from the nozzle #3 bore. These indications were located from 0° to 45°. No other indications were observed on the RCS side of the stainless cladding and nozzle #3 J-groove weld.

The penetrant results for the nozzle #3 bore are shown Figure 3.4.3. A large axial crack was noted in the nozzle #3 bore near the 10° orientation. The 10° orientation was in line with the farthest extent, or nose, of the cavity. Figure 3.4.4 shows the nozzle #3 J-groove weld looking from the top of the RV head. The axial crack near 10° is visible on the top

surface of the J-groove weld, which indicated that the cracking extended completely through the J-groove weld.

### 3.5 Area of Exposed Cladding and Cladding Thickness Measurements

The dental mold (Section 3.2) was used to determine the area of exposed cladding on the lower surface of the cavity. Two different techniques were employed. The first method involved directly tracing the exposed cladding profile onto graph paper, then calculating the area using image analysis. This method yielded an exposed cladding area of 16.5 square inches. For the second method, a photograph was taken of the underside of the dental mold. A gray mask was then digitally applied to the portion of the photograph corresponding to the exposed cladding (Figure 3.5.1). The area was calculated using image analysis and was determined to be 17.3 square inches. The two measurements were in good agreement with each other, but it is believed that the direct tracing method was more reliable since some distortion (i.e., parallax) may have been introduced during photography of the dental mold.

Two opposing dial indicators affixed to a computer numerical controlled (CNC) mill were used to perform the exposed cladding thickness measurements. These dial indicators were initially placed in contact with each other and zeroed. Piece A2 was then secured in the mill (Figure 3.5.2) and the cladding thickness was determined by difference. The thickness measurements were determined in an X-Y grid pattern with a 0.5" spacing. The X-Y origin was selected as the point of maximum upward deflection of the stainless steel cladding (red dot in Figure 3.5.2). The cladding thickness data are shown in Figure 3.5.3. The average thickness of all 78 readings was 0.256", with a minimum reading of 0.202" and a maximum of 0.314". The minimum thickness values occurred near the J-groove weld at the 90° (0.202") and 270° (0.208") locations. The thickness data is presented in a colorized fashion in Figure 3.5.4. It is clear in this figure that the thin cladding (dark blue) was near the 90° and 270° locations. It is also apparent that the weld bead travel was in the 90° to 270° direction (i.e., vertical in the figure). The colorized data for each dial indicator are presented separately in Figure 3.5.5 (upper surface indicator) and Figure 3.5.6 (lower surface indicator). These figures capture the relative height of the cladding, which clearly reached a maximum near the centroid of the exposed cladding. Figure 3.5.7 provides the colorized thickness data superimposed on the exposed cladding macro photograph. The vertical weld bead orientation is again evident.

### 3.6 Additional Visual Inspections

#### *Exposed cladding*

Higher magnification inspections were performed on the exposed cladding after the thickness measurements were complete. Figure 3.6.1 shows the cracking present in the exposed cladding surface. The most pronounced cracking occurred between two cladding weld beads. A higher magnification montage showing the extent of cladding cracking is provided in Figure 3.6.2. Several fine cracks were noted both above (toward 270°) and below (toward 90°) the main cracking. Higher magnification photographs of the main cracks are provided in Figure 3.6.3 and 3.6.4.

### *Cladding underside*

The RCS side of the cladding is shown at low magnification in Figure 3.6.5. The red circle in this figure delineates the deflected portion of the exposed cladding, which is shown at higher magnification in Figure 3.6.6. No cracks were observed on the RCS side of the cladding in the deflected region.

### *Nozzle #3 J-groove Weld*

The nozzle #3 J-groove weld bore near the 10° (downhill side) is shown in Figure 3.6.7. These photos show the extent of the axial cracking at 10°. Looking at the nozzle #3 bore (upper photo in Figure 3.6.7), it can be seen that the axial crack is present from the RCS side of the J-groove weld up to the top of the J-groove weld. The crack is also visible on the top of the J-groove weld (lower photo in Figure 3.6.7), indicating the crack extended completely through the J-groove weld. Axial cracks were also visible on the uphill side of the nozzle #3 bore near the 180° orientation (Figure 3.6.8). These cracks were not as wide or long as the axial crack at 10°.

### *Cavity walls and undercut regions*

The upper portion of the cavity side wall near 90° and 270° is shown in Figure 3.6.9. The side wall striations are most prominent near the nozzle #3 bore near the RV head mid-thickness. These striations become less well defined as the distance from the nozzle #3 bore is increased. In these areas, the side wall exhibits an irregular texture consisting of rather large rounded depressions. Higher magnification photographs of the striations near the nozzle #3 bore are provided in Figure 3.6.10. It appears that the striations are initially parallel to the boric acid solution level in the cavity, then gradually shift parallel to the RV head (i.e., parallel to the stainless steel cladding). A transition from a striated side wall to one containing rounded depressions is shown in the upper photo of Figure 3.6.11. The lower photo in this Figure shows the large rounded depressions present on the upper surface of the cavity nose. The lack of directionality in these depressions suggested that they were formed due to general boric acid corrosion, in the absence of well-defined flow. However, since the as-found cavity walls were some distance away from the axial crack at ~10°, it is possible that erosion may have played a part in the initial cavity formation.

Several regions around the perimeter of the exposed cladding contained undercutting between the cladding and RV head steel. Two such regions are shown in Figure 3.6.12. The presence of these undercut regions indicated a localized galvanic interaction between the cladding and RV steel accelerated the corrosion somewhat. There was no evidence of cracking or disbond associated with these regions.

## 4.0 NON-EXPOSED CLADDING AND LOW ALLOY STEEL TESTING

### 4.1 Sectioning of Block "B"

Figures 4.1.1 and 4.1.2 provide schematic representations of the sections made on block B to create samples for metallography/microhardness and tensile testing. These sections were made using a cooled horizontal band saw or a water-cooled abrasive cut-off saw. The mounted surface of the metallography sample (B2C2B3) was transverse to the weld bead direction (refer to Figure 4.1.2). This metallography sample was prepared in order to collect baseline information regarding the bondline condition between the low alloy steel and stainless steel cladding and characterize the material microstructures and microhardness profile across the interface between the two materials.

Two miniature tensile specimens were machined from the stainless steel cladding using the electrical discharge machining (EDM) technique. These specimens were oriented transverse to the weld bead, with one sample located near the RCS side of the cladding (specimen B2C2A1) and one sample located near the RV head steel (specimen B2C2A2). Refer to Figure 4.1.2 for the sample locations.

### 4.2 Metallography/Microhardness

A macro photograph of the mount containing metallography sample B2C2B3 is provided in Figure 4.2.1. This photo was taken after chemically etching the sample with 2% nital, which revealed the microstructure in low alloy steel. Three distinct regions were present in the carbon steel heat-affected zone (HAZ). The microstructure was acicular near the stainless steel interface and transitioned to a fine-grained structure approximately 0.1" from the interface. A coarse-grained structure was observed approximately 0.3" from the interface. These three microstructures are shown at 100X and 375X in Figures 4.2.2, 4.2.3, and 4.2.4, respectively. Some microstructural banding (indicated by alternating lighter and darker streaks) was also observed in the coarse-grained structure approximately 0.5" from the interface (Figure 4.2.4).

The stainless steel cladding microstructure was revealed by chemically etching with an acetic acid, nitric acid, and hydrochloric acid mixture. At the carbon steel interface, the stainless steel microstructure tends to mimic the carbon steel grain structure, but quickly changes to an elongated dendritic structure 0.002" to 0.003" from the bondline (Figure 4.2.5). The structure was generally consistent throughout the cladding cross section (Figure 4.2.6) and consisted of elongated delta ferrite pools in an austenitic matrix, which is the expected microstructure for Type 308 stainless steel cladding.

A Knoop microhardness profile was taken across the entire specimen width, from the stainless cladding to the low alloy steel. A 500 gram load was used during the test. The hardness indents were spaced nominally 0.010" apart except within 0.060" of the interface, where the readings were spaced 0.005" apart. The microhardness test results are presented along with a low magnification photograph showing the indent locations in Figure 4.2.7. There was some hardness variation noted on the RCS side of the cladding, then the hardness level remained at a consistent HK ~210 until the interface with the low alloy steel. Hardness levels of HK ~300 were noted in the low alloy steel adjacent to the bondline (corresponding to the acicular structure). The hardness readings gradually tapered down

to approximately HK 220-230 approximately 0.5" from the bondline. All of these results appeared consistent with those expected for stainless steel cladding welded to low alloy steel.

#### 4.3 Tensile Testing of Cladding

Miniature tensile specimens were machined from block B to determine the baseline mechanical properties for the stainless steel cladding. A photograph of a dummy specimen is shown in Figure 4.3.1 to illustrate the specimen design. This design is a sub-size flat bar type sample, measuring 0.080" thick by 0.200" in the reduced area. Overall specimen length is 2.5". The specimen is secured in the tensile test fixture by inserting pins through the holes on both ends of the specimen. The test temperature for both specimens was 600° F.

The specimens were machined from the same area of cladding, with one specimen located closer to the RCS side of the cladding and the other specimen located closer to the low alloy steel RV head. The intent of this sample configuration was to determine if a mechanical property gradient existed across the stainless steel cladding thickness. The engineering stress-strain curves for the two specimens are presented in Figure 4.3.2 along with the tabulated data for ultimate tensile strength, 0.2% offset yield strength, % elongation, and % reduction in area. The results for both specimens were considered to be within experimental scatter, so it was concluded that no mechanical property gradient was present. The data indicated a tensile strength of ~56 ksi, yield strength of ~31 ksi, 28.7% elongation, and ~37% reduction in area. Photographs of the two specimens taken after the test are provided in Figures 4.3.3 and 4.3.4. These photographs show the break location, which was within the gage length for both specimens. Also noted was ductile necking adjacent to the fracture surfaces.

#### 5.0 SECTIONING OF CAVITY

Several sections were required on the cavity sections (pieces A1 and A2) to produce samples suitable for metallography and SEM/EDS examinations. Figure 5.1 through 5.12 provide details related to the sectioning of piece A2; Figure 5.13 through Figure 5.16 detail the sections made on piece A1. In order to maintain sample identifications, an alphanumeric identification system was employed. For example, when piece A1 was sectioned into four smaller pieces these pieces were identified as pieces A1A, A1B, A1C, and A1D. Additional sections made on piece A1B created pieces A1B1, A1B2, A1B3, A1B4, A1B5, A1B6, and A1B7. To determine the original location of a particular sample, simply refer to the first few letters of the sample identification.

In addition, each figure is accompanied by a table. The table and corresponding figure are numbered identically, so Figure 5.1 is accompanied by Table 5.1. The tables provide the sample identifications, locations, test plan, and the number of metallographic and/or SEM/EDS samples prepared from the sample (as applicable).

Extensive sectioning was performed on piece A2 (Table 5.1 and Figure 5.1). These cuts were made to isolate the axial J-groove weld cracking at 180° (piece A2A2), the thin area of cladding (piece A2A5), the axial cracking near 10° and circumferential cracking at 0°-45° (piece A2A6), and the exposed cladding cracks and undercut regions (A2A7). Further

sectioning details on these four pieces is provided in Figure/Table 5.2 through Figure/Table 5.12.

The upper portion of the cavity (piece A1) was sectioned to permit metallographic and SEM inspections of the cavity side wall near the 90° (piece A1B) and 270° (piece A1D) locations. For each orientation, a metallographic mount was prepared through the upper and lower portion of the striated cavity side wall. In addition, the middle portion of the cavity side wall (between the two metallographic mounts) was examined by SEM. Sectioning details for pieces A1B and A1D are provided in Figure/Table 5.14 through Figure/Table 5.16.

## 6.0 EXPOSED CLADDING TESTING

Four metallographic mounts were prepared through areas of exposed cladding to assess the cladding thickness, crack depth and morphology, cladding hardness, and cladding microstructure. Refer to Figure 5.11 for the sample and mounting surface orientations. For these samples, the cladding microstructure was revealed by swab etching 30-45 seconds in an acetic-nitric-hydrochloric acid solution. Three of the mounts were also examined by SEM/EDS primarily to determine if any chemical composition gradients existed (especially chromium) across the cladding thickness. The main portion of the cracking (shown in Figures 3.6.1 and 3.6.2) was opened up in the laboratory to permit SEM/EDS examination of the fracture surface. Refer to Figures 5.11 and 5.12 for the sample orientation. The thin area of cladding near the 90° orientation was examined to determine if the thinning was due to corrosion or a stainless cladding deposition technique change (i.e., automated six-wire process to a manual single wire process). Refer to Figures 5.1 and 5.3 for the sample and mounting surface orientations.

### 6.1 Near Center Crack (Sample A2A7M)

#### 6.1.1 Metallography/Microhardness

The sample prepared through the cladding near the center crack was designated sample A2A7M and was shown previously in Figure 5.11. A low magnification photograph of the metallographic mount is provided in Figure 6.1.1.1 along with the Knoop microhardness data. In the macro photo, the microhardness traverse is visible as are several cracks that initiated in the exposed cladding. The Knoop microhardness results indicated a slight hardness elevation near the exposed cladding surface (~270-300 HK). Otherwise, the hardness level was fairly uniform throughout the cladding cross section and averaged approximately 225 HK. The cladding thickness in this sample ranged from 0.227" to 0.277". In the area containing the deepest cracking, the distance from the crack tip to the RCS side of the cladding was approximately 0.199".

Micrographs showing the typical cladding microstructure on the exposed surface are provided in Figure 6.1.1.2. These micrographs show the shallow intergranular attack (1-2 grains deep) and intergranular/interdendritic cracking present in this area. Micrographs showing the deepest observed cracking are shown in Figure 6.1.1.3. In this area, the cracking extended approximately 0.057" below the exposed cladding surface. The crack morphology was intergranular or interdendritic. Micrographs showing the typical microstructures near the mid-thickness of the cladding are presented in Figure 6.1.1.4. The microstructure was as expected for Type 308 stainless steel cladding and consisted of

elongated delta ferrite pools in an austenite matrix. Micrographs taken on the RCS side of the cladding are provided in Figure 6.1.1.5. There was no evidence of intergranular attack or cracking present on the RCS side of the cladding.

### 6.1.2 SEM/EDS

The SEM/EDS results for this sample are given in Figures 6.1.2.1 and 6.1.2.2. Line scans (not included in this report) for several elements were taken across the cladding thickness. The data indicated that there were no significant chemical composition variations through the thickness. The line scan data was not quantified, therefore three separate area EDS spectra were collected from the cladding cross section: one near the exposed cladding surface (area 1), mid-thickness (area 2), and near the RCS side (area 3). Of particular interest was the chromium content, which remained consistent through the cladding cross section: area 1 - 18.36%, area 2 - 18.01%, and area 3 - 18.16%. Similar results were obtained for the other elements; refer to the tabulated data in Figure 6.1.2.1. Higher magnification micrographs showing the deepest crack are provided in Figure 6.1.2.2. It is clear from these micrographs that the crack propagated in an interdendritic fashion and preferentially along the elongated ferrite pools.

## 6.2 ~1/2" from Center Crack toward 270° (Sample A2A7N)

### 6.2.1 Metallography

A low magnification photograph of the metallographic mount prepared approximately 1/2" from the main center crack toward the 270° orientation is provided in Figure 6.2.1.1. The cladding thickness in this sample ranged from 0.228" to 0.282". In the area containing the deepest cracking, the distance from the crack tip to the RCS side was approximately 0.188". A micrograph showing a crack propagating approximately 0.036" into the cladding is shown in Figure 6.2.1.2. Higher magnification micrographs showing the exposed cladding surface are presented in Figure 6.2.1.3. Similar to the previous sample, a shallow layer (1-2 grains deep) of intergranular attack (IGA) was present on the exposed cladding surface. Micrographs showing the typical cladding microstructure near the mid-thickness are shown in Figure 6.2.1.4. These micrographs are similar to those previously reported and are consistent with Type 308 stainless steel cladding. There was no evidence of cracking on the RCS side of this sample (Figure 6.2.1.5).

### 6.2.2 SEM/EDS

A low magnification BSE micrograph showing the full cladding thickness is provided in Figure 6.2.2.1 along with EDS spectra collected from the exposed cladding surface, mid-thickness, and near the RCS side of the cladding. The crack depth in this area ranged from 0.035" to 0.053" below the exposed cladding surface. The distance from the crack tip of the deepest crack to the RCS side of the cladding was approximately 0.208". The EDS data indicated no significant variation in the chromium content across the cladding thickness: 17.62% on the exposed side, 18.05% at the mid-thickness, and 18.21% on the RCS side. Other major elements were generally uniform across the cladding thickness as well. Higher magnification SE and BSE micrographs of the deepest crack tip are presented in Figure 6.2.2.2. The crack morphology is clearly interdendritic and propagates along the elongated ferrite pools.

### 6.3 ~3/4" from Center Crack toward 90° (Sample A2A7S)

#### 6.3.1 Metallography/Microhardness

A low magnification photograph of the metallographic mount prepared though the cladding approximately 3/4" from the main center crack toward the 90° orientation is shown in Figure 6.3.1.1. In this area, the cladding thickness ranged from 0.257" to 0.287" and the crack depth ranged from 0.039" to 0.052". The distance from the crack tip of the deepest crack to the RCS side of the cladding was approximately 0.211". The Knoop microhardness profile taken across the cladding thickness indicated a lower hardness (<200 HK) toward the exposed cladding surface, which was in contrast to the hardness increase (270-300 HK) observed on the exposed cladding surface near the main crack. Away from the exposed cladding surface, this sample exhibited an average hardness of approximately 225 HK, which is consistent with the results obtained near the main crack.

Micrographs taken of the shallow IGA present on the exposed cladding surface is shown in Figure 6.3.1.2. As with the previous samples, there were several IGA penetrations present on the surface that extended 1-2 grains deep into the cladding. Examples of the deepest cracks are provided in Figure 6.3.1.3. The cracking initiated at the shallow IGA and propagated along an interdendritic path. Microstructures taken near the cladding mid-thickness (Figure 6.3.1.4) and on the RCS side (6.3.1.5) were similar to the previous samples, and were consistent with those expected for Type 308 stainless steel cladding. No evidence of cracking was noted on the RCS side of the cladding.

#### 6.3.2 SEM/EDS

The three EDS spectra collected from the cladding cross section are presented along with the reference micrograph in Figure 6.3.2.1. As noted previously, there was no significant chemical composition gradient noted across the cladding thickness. The chromium contents for this sample were as follows: 18.41% on exposed surface, 18.24% near mid-thickness, and 18.46% near RCS side. The other major elements exhibited a relatively uniform composition also. Higher magnification BSE and SE micrographs of the deepest crack tip are provided in Figures 6.3.2.2 and 6.3.2.3. These micrographs illustrate the interdendritic nature of the crack path.

### 6.4 Main Crack Opened Up (Sample A2A7L)

#### 6.4.1 SEM/EDS

A low magnification mosaic of one half of the open crack sample is presented in Figure 6.4.1.1. The exposed cladding surface is located along the lower edge of this figure. Letters A through E indicate the areas of the fracture surface selected for higher magnification inspections. Higher magnification micrographs of area A are shown in Figure 6.4.1.2. Heavy deposits were present on the fracture surface (darker contrast regions in the BSE imaging mode). In areas containing fewer deposits, the observed fracture morphology was interdendritic. Area B micrographs are provided in Figure 6.4.1.3. The elongated nature of the grain structure is apparent at low magnifications; at higher magnifications, the fracture surface was mixed intergranular/interdendritic. Similar results were obtained for area C (Figure 6.4.1.4), which contained surface deposits and a region of

ductile tearing created in the laboratory. The in-service cracking was mixed intergranular/interdendritic. The fracture surface appearance near area D (Figure 6.4.1.5) was similar to area C and consisted of an elongated dendritic structure with interdendritic/intergranular cracking. The ductile portion of the fracture surface was created in the laboratory. Area E (Figure 6.4.1.6) also contained interdendritic/intergranular cracking and heavy surface deposits. The deposits near area E were examined by EDS to qualitatively assess their chemical composition. The first deposit region (Figure 6.4.1.7) contained primarily carbon, oxygen, iron, aluminum, silicon, and chromium. Possible trace levels of nickel and chlorine were detected as well. The results for the second deposit region are shown in Figure 6.4.1.8. These grain boundary deposits contained carbon, oxygen, silicon, chromium, iron, and nickel. Lesser amounts of aluminum, sulfur, and calcium were also detected.

## 6.5 Mounted Sample through Thin Area of Cladding near 90° (Sample A2A5C)

### 6.5.1 Metallography/Microhardness

A low magnification photograph of the metallographic mount prepared through the thin area of cladding near 90° is presented in Figure 6.5.1.1. In this area, the minimum measured cladding thickness was 0.179". Two microhardness traverses were made across this sample: one through the thick portion of exposed cladding (left side of macro photograph) and one through the low alloy steel stainless steel interface (right side of photograph). The hardness readings in the exposed cladding were generally consistent and averaged between 250-300 HK. In the unexposed cladding, the hardness levels were somewhat lower (200-250 HK). Some hardness variation was observed near the low alloy steel stainless steel fusion line. A low magnification photograph of the metallographic mount after chemical etching is presented in Figure 6.5.1.2. The uniform microstructure of the stainless steel cladding indicated that no weld process change occurred in this region.

A higher magnification micrograph taken near the undercut region of this sample is provided in Figure 6.5.1.3. It appeared that some additional corrosion occurred due to the galvanic interaction between the stainless steel cladding and the low alloy steel RV head material. There was no evidence of disbond between the stainless steel and low alloy steel associated with this undercutting. The typical appearance of the bondline is shown in Figure 6.5.1.4. Micrographs taken of the exposed cladding portion of this sample are shown in Figure 6.5.1.5. These micrographs highlight the shallow (1-2 grains deep) IGA noted on other exposed cladding samples. Micrographs showing the typical cladding microstructure is this sample are presented in Figure 6.5.1.6. The microstructure is as expected and contained a dendritic structure delineated by elongated ferrite pools in an austenite matrix.

## 7.0 NOZZLE #3 J-GROOVE WELD TESTING

Metallographic mounts were prepared through areas of the J-groove weld to assess the crack depth and morphology of axial cracks identified at the ~180° (uphill) and ~10° (downhill) orientations and short circumferential cracks between ~0° and ~45° on the RCS side of the weld. The microstructure of the Alloy 182 J-groove weld was revealed by electrolytically etching with oxalic acid.

## 7.1 Axial Crack near 180°

### 7.1.1 Metallography/Microhardness

A low magnification photograph of the metallographic mount prepared through the crack on the uphill side of the nozzle #3 bore is presented in Figure 7.1.1.1. Refer to Figures 5.1 and 5.2 for the sample and mounting surface orientations. Three axial cracks are visible in the mount, with the deepest crack extending approximately 0.24" below the nozzle #3 bore I.D. surface. The Knoop microhardness profile, which is also visible in the macro photograph, indicated a relatively uniform hardness of approximately 250 HK, except near the nozzle bore I.D. surface where the hardness level increased to ~300 HK. This hardness increase was due to the cold work generated during the boring to remove the nozzle. Higher magnification micrograph mosaics of the largest crack are provided in the as-polished and etched conditions in Figure 7.1.1.2. The cracking is clearly intergranular or interdendritic in nature, with some minor crack branching. A micrograph showing the typical microstructure of the J-groove weld is shown in Figure 7.1.1.3. The grain size and dendritic structure appeared consistent with that expected for Alloy 182 weld metal. Higher magnification micrographs taken of the crack tips are provided in Figure 7.1.1.4. As noted previously, the cracking is mixed intergranular/interdendritic. Higher magnification micrographs taken near the nozzle #3 bore I.D. surface (Figure 7.1.1.5) illustrate the shallow cold work layer.

## 7.2 Axial Crack near ~10°

The axial crack on the downhill side of the nozzle extended from the RCS side of the J-groove weld to the top (exposed) surface of the J-groove weld. Metallographic mounts were prepared through the upper and lower portion of the J-groove weld; SEM/EDS analysis was conducted on an opened-up portion of the crack near its mid-thickness. SEM/EDS analysis was also performed on the mounted sample prepared through the upper portion of the crack. Refer to Figures 5.1, 5.4, 5.5, 5.6, and 5.10 for the sample and mounting surface locations.

### 7.2.1 Metallography of Upper Portion of Crack

A low magnification photograph of the metallographic mount prepared through the upper portion of the crack is shown in Figure 7.2.1.1. In this area, the cracking extends entirely through the weld cross section (crack length ~0.75"), which is in contrast to the cracking on the uphill side that extended ~0.24" into the J-groove weld. At slightly higher magnification (lower micrograph in Figure 7.2.1.1), the crack is tighter near its initiation on the nozzle bore I.D. compared to the end of the crack, which is much wider. This crack widening was likely due to the flow of leaking primary coolant through the crack. Higher magnification detail micrographs of the crack are provided in Figure 7.2.1.2. The cracking exhibits branching and is mixed intergranular/interdendritic in nature. A micrograph showing the typical microstructure of the J-groove weld is shown in Figure 7.2.1.3. This microstructure was similar to the microstructure observed near 180° (Figure 7.1.1.3) and was consistent with that expected for Alloy 182 weld material.

### 7.2.2 SEM/EDS of Upper Portion of Crack (Mounted Sample)

The mounted sample prepared through the upper portion of the crack was also examined by SEM/EDS. Figure 7.2.2.1 provides results for a wide portion of the crack. The EDS spectrum collected from deposits in the crack indicated high concentrations of carbon, oxygen, iron, and nickel. Lesser amounts of chromium, manganese, zirconium, aluminum, silicon, and titanium were also detected. These results indicated that corrosion products from the low alloy steel RV head became entrapped within the crack. EDS results were also obtained from a thin layer adjacent to the crack face. This area, which is shown in Figure 7.2.2.2, appeared to be a film on the crack face rather than deposits. The darker contrast in the BSE imaging mode indicated that this film consisted of lower atomic number constituents compared to the bulk weld metal. The EDS spectrum results indicated high concentrations of carbon, oxygen, niobium, titanium, chromium, manganese, iron, and nickel. Lesser amounts of aluminum, silicon, tin, and calcium were also detected.

### 7.2.3 Metallography of Lower Portion of Crack

A low magnification photograph taken of the metallographic mount prepared through the lower portion of the axial crack at 10° is presented in Figure 7.2.3.1. In this plane, the cracking extended partly through the J-groove weld (crack length ~0.45"). Crack branching is evident at low magnification, as are two weld voids measuring ~0.035" and ~0.070" in diameter. A higher magnification micrograph mosaic of the crack is provided in Figure 7.2.3.2. Cracking appears branched and intergranular/interdendritic in nature. The center portion of this mosaic contains open parallel cracks with an appearance similar to hot cracking. However, no other instances of this crack morphology were noted anywhere else in this sample (i.e., away from the main crack), therefore it is unlikely that hot cracking was responsible for the cracking in this area. A two-frame micrograph mosaic taken near the nozzle #3 bore I.D. surface is shown in Figure 7.2.3.3. The shallow cold work layer from the nozzle removal process is visible. Higher magnification micrographs showing cracking details are presented in Figure 7.2.3.4. Cracking is highly branched and mixed interdendritic/intergranular in nature. Micrographs taken near the crack tips are provided in Figures 7.2.3.5 and 7.2.3.6. Some crack widening is observed near the crack tip, which was likely the result of leaking primary coolant passing through the crack.

### 7.2.4 SEM/EDS of Middle Portion of Crack (Open Crack Sample)

The middle portion of the axial crack at ~10° was opened up in the laboratory to permit visual inspection by SEM/EDS. A low magnification photograph showing the open-up sample is provided in Figure 7.2.4.1. The open crack sample was affixed to a 1" diameter aluminum SEM stub using black double-sided adhesive tape. The fracture surface is coated with dark gray to black deposits near the nozzle #3 bore and brown deposits near the weld mid-thickness. Fresh fracture due to opening in the laboratory is present on the outer edge of the J-groove weld fracture surface. A low magnification SEM mosaic taken of one half on the fracture surface is presented in Figure 7.2.4.2. This figure is annotated with the main fracture surface features, which included interdendritic cracking near the nozzle bore I.D. surface, a heavily deposited/oxidized region near the weld mid-thickness, and fresh ductile tearing from opening up the crack. A higher magnification micrograph taken near the nozzle bore is shown in Figure 7.2.4.3. The elongated grain structure and interdendritic nature of the cracking is evident. The fracture mode was indeterminate in the

heavily deposited portion of the fracture surface (Figure 7.2.4.4). Toward the crack tip (Figure 7.2.4.5), the fracture mode was mixed interdendritic (in-service cracking) and ductile tearing (lab fracture). EDS spectra were collected from the three regions shown in the low magnification BSE mosaic in Figure 7.2.4.6. Note the darker contrast of the in-service fracture compared to the laboratory fracture (upper right of mosaic). This contrast difference is indicative of a heavy oxide layer on the in-service fracture surface. Near the crack initiation (area 1), the primary elements detected were carbon, oxygen, silicon, chromium, manganese, iron, nickel, and zirconium. At the crack mid-thickness (area 2), the elements included those detected at area 1, plus aluminum, titanium, and tin. Similar results were obtained near the crack tip (area 3), except area 3 also contained niobium and calcium.

### 7.3 Circumferential Cracking from $\sim 0^\circ$ to $\sim 45^\circ$ on RCS Side

Two metallographic mounts and one open crack sample were prepared from the RCS side of the J-groove weld containing circumferential cracking. These cracks, which were short and discontinuous in nature, were located between  $\sim 0^\circ$  and  $\sim 45^\circ$ . The metallographic samples were prepared from the  $20^\circ$  and  $45^\circ$  orientations and the open crack sample was located near  $30^\circ$ . The open crack sample and the mounted sample at  $20^\circ$  were examined by SEM/EDS. Refer to Figures 5.1, 5.4, 5.5, 5.6, 5.7, 5.8, 5.9, and 5.10 for the sample and mounting surface orientations.

#### 7.3.1 Metallography near $45^\circ$

Low magnification photographs of the mounted metallographic mount prepared through the circumferential cracking near  $45^\circ$  are shown in Figures 7.3.1.1 and 7.3.1.2. This sample contains both the cladding and a portion of the J-groove weld. The shallow circumferential cracks are visible on the RCS side of the J-groove weld. Interestingly, deeper cracks were observed on the exposed cladding surface extending to the J-groove weld. These cracks are shown at higher magnification in Figure 7.3.1.3. Cracking follows the elongated ferrite structure in the stainless steel cladding and extends into the J-groove weld, where the crack changes direction and follows the elongated structure of the J-groove weld (Figure 7.3.1.4). Also observed was corrosion attack on the exposed surface of the J-groove weld due to exposure to the boric acid slurry. The circumferential cracking is shown in Figure 7.3.1.5. These cracks were shallow ( $\sim 0.019$ " deep) and were confined to a thin weld bead applied to the RCS side of the J-groove weld. At higher magnification (Figure 7.3.1.6) the observed crack morphology is interdendritic or intergranular with some minor branching near the crack tip. The wider regions present just below the crack initiation may have been dendrites or grains that became encircled by the cracks and subsequently dropped out during sample preparation. Higher magnification micrographs of the circumferential crack tips are presented in Figure 7.3.1.7. The typical J-groove weld microstructure is provided in Figure 7.3.1.8. This microstructure is consistent with those observed previously and was typical for Alloy 182 weld material.

#### 7.3.2 Metallography near $20^\circ$

A low magnification photograph of the mounted sample prepared through the circumferential cracking near  $20^\circ$  is presented in Figure 7.3.2.1. This sample contained shallow ( $0.018$ " deep) circumferential cracking on the RCS side of the J-groove weld and

cracking initiating on the exposed surface of the cladding and extending toward the J-groove weld interface. The circumferential cracking is shown at higher magnification in Figure 7.3.2.2. Similar to the previous sample, the cracking was confined to a thin weld bead applied to the RCS side of the J-groove weld. The cracking at this location also exhibited a widening just below the crack initiation, which may have been caused by dendrites dropping out during sample preparation. Cracking was mixed intergranular/interdendritic in nature. Micrographs taken of the cracking located on the exposed surface of the cladding are presented in Figure 7.3.2.3. In this location, it appeared the cracking followed an interdendritic path through the stainless steel cladding along the stainless/J-groove weld interface. The cracking did not penetrate the J-groove weld. Also noted was a uniform corrosion attack on the exposed J-groove weld surface (Figure 7.3.2.4). This attack was likely caused by exposure to the oxygenated boric acid in the cavity.

### 7.3.3 SEM/EDS near 20° (Mounted Sample)

A low magnification BSE micrograph of the mounted sample prepared through the circumferential cracking present near 20° is presented in Figure 7.3.3.1. Note the darker contrast of the stainless steel cladding (i.e., lower atomic number) compared to the Alloy 182 J-groove weld (higher atomic number). The circumferential cracking and the cracking initiating at the exposed cladding surface are visible. An EDS spectrum was collected from area 1 to semi-quantitatively determine the J-groove weld chemical composition. The results of this analysis, which are provided in Figure 7.3.3.2, were consistent with the specified requirements for Alloy 182. A higher magnification BSE micrograph of the exposed cladding cracking is presented in Figure 7.3.3.3. As noted previously, the cracking progresses in an interdendritic fashion along the stainless/J-groove weld interface and does not penetrate the J-groove weld. The circumferential cracking on the RCS side of the J-groove weld is shown at higher magnification in Figure 7.3.3.4. Some entrapped particles (aluminum oxide, silicon carbide, and mounting compound) were detected in these cracks by EDS. These particles were likely introduced during sample preparation.

### 7.3.4 SEM/EDS near 30° (Open Crack Sample)

The circumferential cracks located near the 30° orientation were opened up in the laboratory for SEM analysis. Figure 7.3.4.1 is a low magnification photograph of the open crack sample mounted on the SEM sample stub. Figure 7.3.4.2 provides two SE micrographs showing the interdendritic nature of the cracking.

## 8.0 CAVITY WALL AND UNDERCUT REGIONS

Inspections of the cavity side wall focused on the striated portions of the cavity toward the 90° and 270° directions. For each orientation, a metallographic mount was prepared from the upper and lower areas of the cavity. The middle portion of the cavity wall was examined under the SEM. A 2% nital etching solution was used to reveal the microstructure of the low alloy steel. At the 270° location, a macro etch test was performed to assess the degree of banding present in the low alloy steel microstructure. For this examination, a 10% nital solution was used. Refer to Figures 5.13 through 5.16 for the sample and mounting surface locations.

### 8.1 Cavity Wall Inspections near 90°

#### 8.1.1 Metallography of Upper Portion of Cavity Wall

Figure 8.1.1.1 provides a low magnification photograph of the upper portion of the cavity wall toward the 90° orientation. At higher magnifications (Figures 8.1.1.2 and 8.1.1.3) the banded microstructure of the low alloy steel is evident. This banding, which is aligned with the major axis of the low alloy steel plate, is typical for SA-533, Gr. B (mod), Cl. 1 low alloy steel plate and is attributed to carbide segregation within the microstructure. It appeared that the corrosion of the side wall may have been accelerated slightly due to the banded structure. A higher magnification micrograph showing the typical tempered martensite microstructure of the low alloy steel is provided in Figure 8.1.1.4.

#### 8.1.2 Metallography of Lower Portion of Cavity Wall

Figure 8.1.2.1 presents a low magnification photograph of the metallographic mount prepared through the lower portion of the cavity side wall near 90°. At higher magnifications (Figures 8.1.2.2 and 8.1.2.3), it appeared that the banded microstructure accelerated the corrosion in some cases, but not all. In fact, the heaviest banding (near the center on Figure 8.1.2.2) did not have any localized corrosion associated with it. The typical microstructure is provided in Figure 8.1.2.4. This structure is identical to the one shown previously in Figure 8.1.1.4 for the upper portion of the cavity.

#### 8.1.3 SEM of Middle Portion of Cavity Wall

Low magnification SE micrographs taken near the middle portion of the cavity near the 90° location are presented in Figure 8.1.3.1. The surface was covered with rounded depressions measuring approximately 0.039" or less in diameter. The lack of directionality in these depressions indicated the influence of flow on their formation was minimal. Smaller depressions (~0.015") were caused by inclusions. Higher magnification micrographs taken in this area are shown in Figures 8.1.3.2 and 8.1.3.3. These micrographs illustrate the heavy deposits present on the cavity side wall.

## 8.2 Cavity Wall Inspections near 270°

### 8.2.1 Macro Etch Test

A macro etch test was performed on the low alloy steel near the 270° orientation in two orthogonal directions: parallel to the cavity side wall and perpendicular to the cavity sidewall. Prior to chemical etching, the surfaces were ground with 400 grit paper. Figure 8.2.1.1 presents the results of this test. It appeared that the degree of banding was more pronounced in the surface perpendicular to the cavity sidewall. Banding in this grade of low alloy steel is attributed to carbide segregation within the microstructure. It appeared that two heavily banded areas on this surface corresponded well with prominent corrosion grooves on the cavity side wall surface.

### 8.2.2 Metallography of Upper Portion of Cavity Wall

Figure 8.2.2.1 presents a low magnification photograph of the metallographic mount prepared through the upper portion of the cavity side wall near the 270° orientation. At higher magnifications (Figures 8.2.2.2 and 8.2.2.3), the structure was banded and similar to that previously observed near 90°. Some of the deepest grooves in this area appear to align with banded microstructure. The typical microstructure for this area is provided in Figure 8.2.2.4. This microstructure is consistent with the tempered martensite structure in low alloy steels.

### 8.2.3 Metallography of Lower Portion of Cavity Wall

A low magnification photograph of the metallographic mount prepared through the lower portion of the cavity side wall near the 270° orientation is presented in Figure 8.2.3.1. The higher magnification micrographs shown in Figures 8.2.3.2 and 8.2.3.3 indicate a correlation between the deepest corrosion grooves and the microstructural banding. The typical microstructure in this area is provided in Figure 8.2.3.4.

### 8.2.4 SEM of Middle Portion of Cavity Wall

Figure 8.2.4.1 provides low magnification SE and BSE images of the middle portion of cavity side wall near 270°. The surface in this area was covered with small rounded depressions measuring 0.020" or less in diameter. As noted previously, the rounded nature of these depressions indicated the influence of flow in their formation was minimal. Higher magnification micrographs documenting the appearance of cavity wall surface deposits are provided in Figures 8.2.4.2 and 8.2.4.3.

## 8.3 Examination of Undercut Regions

### 8.3.1 Metallography near 345°

A low magnification photograph showing the undercut sample prepared through the 345° location is presented in Figure 8.3.1.1. The undercut notch is visible at the low alloy steel stainless steel interface. A higher magnification micrograph of the undercutting is shown in Figure 8.3.1.2. There was no evidence of disbond or cracking associated with this area. An example of IGA and intergranular/interdendritic cracking on the exposed surface of the

cracking (away from the undercut notch) is provided in Figure 8.3.1.3. This cracking extended approximately 0.047" below the exposed cladding surface. Micrographs showing the shallow IGA present on the exposed cladding surface are shown in Figure 8.3.1.4. The shallow cracking follows an interdendritic/intergranular path. The bondline between the stainless steel and low alloy steel was acceptable, with no evidence of cracking or disbond (Figure 8.3.1.5). Typical cladding microstructures are provided in Figure 8.3.1.6.

### 8.3.2 Metallography near 10° (Nose of Cavity)

A low magnification photograph showing the metallographic mount prepared through the nose of the cavity near 10° is provided in Figure 8.3.2.1. A higher magnification two-frame mosaic of the nose region is shown in Figure 8.3.2.2. As noted in the previous sample, there was no evidence to cracking or disbond associated with the stainless steel low alloy steel interface. Shallow regions of IGA and interdendritic/intergranular cracking were observed on the exposed cladding surface (Figure 8.3.2.3). The maximum crack depth in this area was approximately 0.024". The bondline between the stainless steel and low alloy steel (Figure 8.3.2.4) and the cladding microstructure (Figure 8.3.2.5) were acceptable.

### 8.3.3 Metallography near 40°

A low magnification photograph showing the sample prepared through the undercut region near 40° is shown in Figure 8.3.3.1. Pronounced undercutting was present in this area, which is shown at higher magnification in Figure 8.3.3.2. There did not appear to be any cracking or disbond associated with the undercutting in this area. Once again, shallow IGA and cracking were observed on the exposed cladding surface (Figure 8.3.3.3). Micrographs documenting the stainless steel low alloy steel bondline and the cladding microstructure are presented in Figures 8.3.3.4 and 8.3.3.5, respectively.

## 9.0 SUMMARY AND CONCLUSIONS

- Visual inspections on the lower end of CRDM nozzle #2 revealed no evidence of cracking. It is believed that the cracks were bored out during the removal process.
- The axial cracking on the uphill side of CRDM nozzle #3 was typical of primary water stress-corrosion cracking (PWSCC) in Alloy 600. This cracking initiated on the nozzle I.D. surface and propagated in an intergranular fashion. The large grain size (ASTM 3) and the discontinuous intergranular carbide distribution contributed to the PWSCC susceptibility of this heat of material.
- The axial cracks in the nozzle #3 J-groove weld on both the uphill and downhill sides were typical of PWSCC in Alloy 182. Cracking in these areas progressed in an interdendritic or intergranular fashion. Cracking was more pronounced on the downhill side, which corresponded to the large corrosion cavity location. The wider opening observed on the axial crack on the downhill side was likely due to the flow of primary coolant leaking through the crack. There was no conclusive evidence that hot cracking contributed to the J-groove weld cracking.
- The exposed cladding surface area was approximately 16.5 square inches. The average cladding thickness measured by dial calipers was 0.256", with a minimum thickness of 0.202" and maximum thickness of 0.314". Thickness measurements taken on a transverse metallographic mount prepared through the thinnest portion of exposed cladding indicated a minimum cladding thickness of 0.179". This area, which was located in an uncracked region of the cladding adjacent to the J-groove weld, was not accessible during the dial caliper measurements. The cladding mechanical properties and chemical composition appeared uniform across the cladding thickness. The underside (RCS side) of the cladding and the unexposed portions of cladding did not contain any cracks or other signs of deterioration.
- Shallow intergranular attack (IGA) was observed on all exposed cladding surfaces examined. Deeper cracks, which extended a maximum 0.057" below the exposed cladding surface, followed a mixed interdendritic/intergranular path. These cracks initiated in the IGA and propagated under a stress-corrosion cracking mechanism along the ferrite stringers under the influence of an applied tensile stress (i.e., system pressure). The minimum observed distance from an exposed cladding crack tip to the RCS side of the cladding was 0.188".
- The striations on the cavity side wall appear to be influenced by boric acid solution level initially and the RV head microstructure afterward. The banded microstructure of the low alloy steel plate showed good correlation with the preferential corrosion that produced the striated texture. There was no evidence of erosion present on the as-found cavity walls; however, erosion may have played a part in the initial cavity formation.
- The undercut regions observed around the perimeter of the exposed cladding were due to localized galvanic corrosion between the low alloy steel and the stainless steel. There was no evidence of cracking or disbond associated with any of these areas.

## 10.0 REFERENCE

1. "Specification for Nickel-Chromium-Iron Alloy Seamless Pipe and Tube," American Society of Mechanical Engineers Boiler and Pressure Vessel Code Section II, Part B, SB-167, ASME, New York, NY (1965).

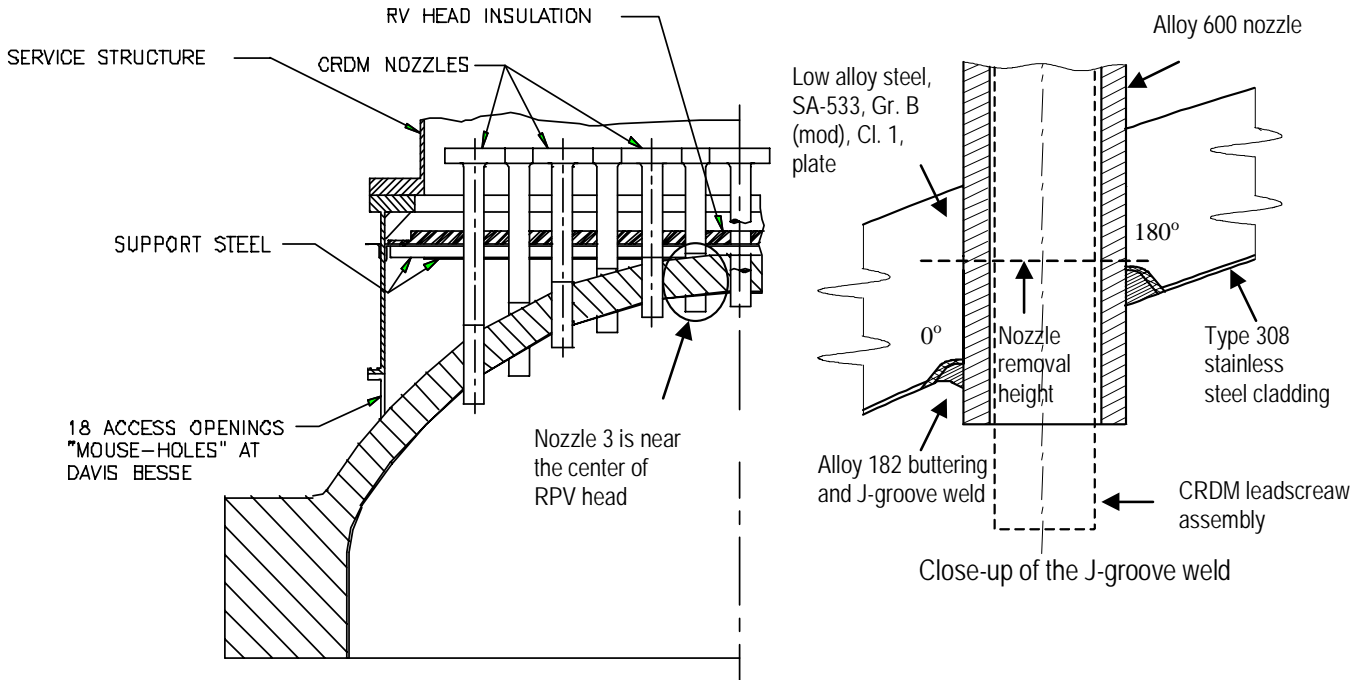


**Figure 1.1.1: Schematic diagrams showing the Davis-Besse RV head and J-groove welding configuration (not to scale).**

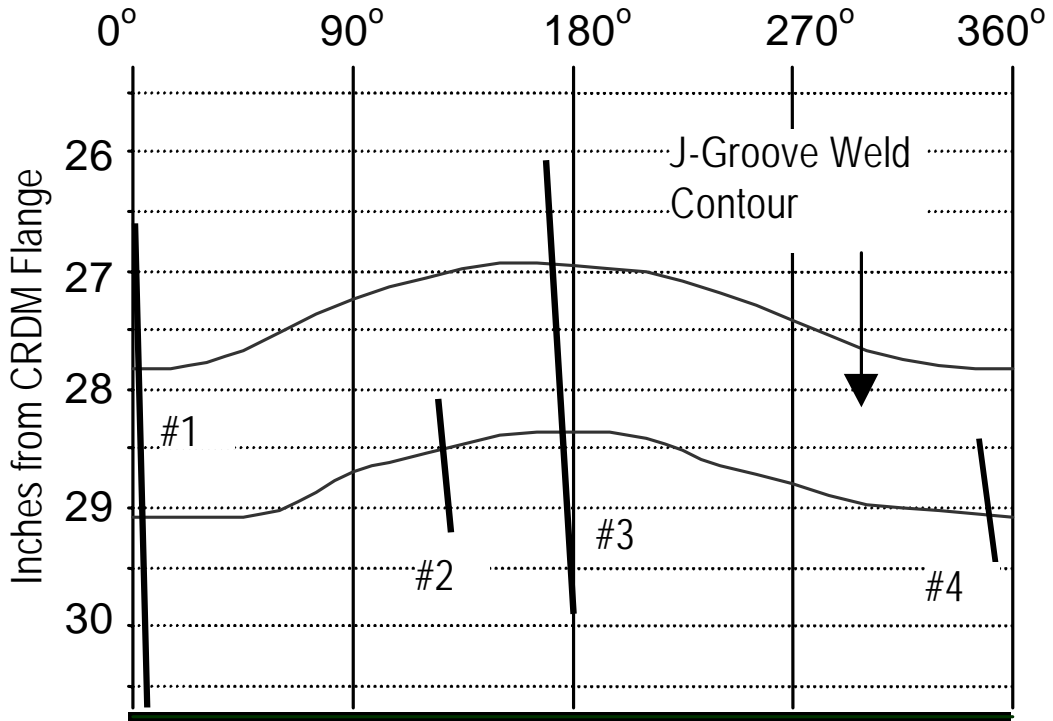
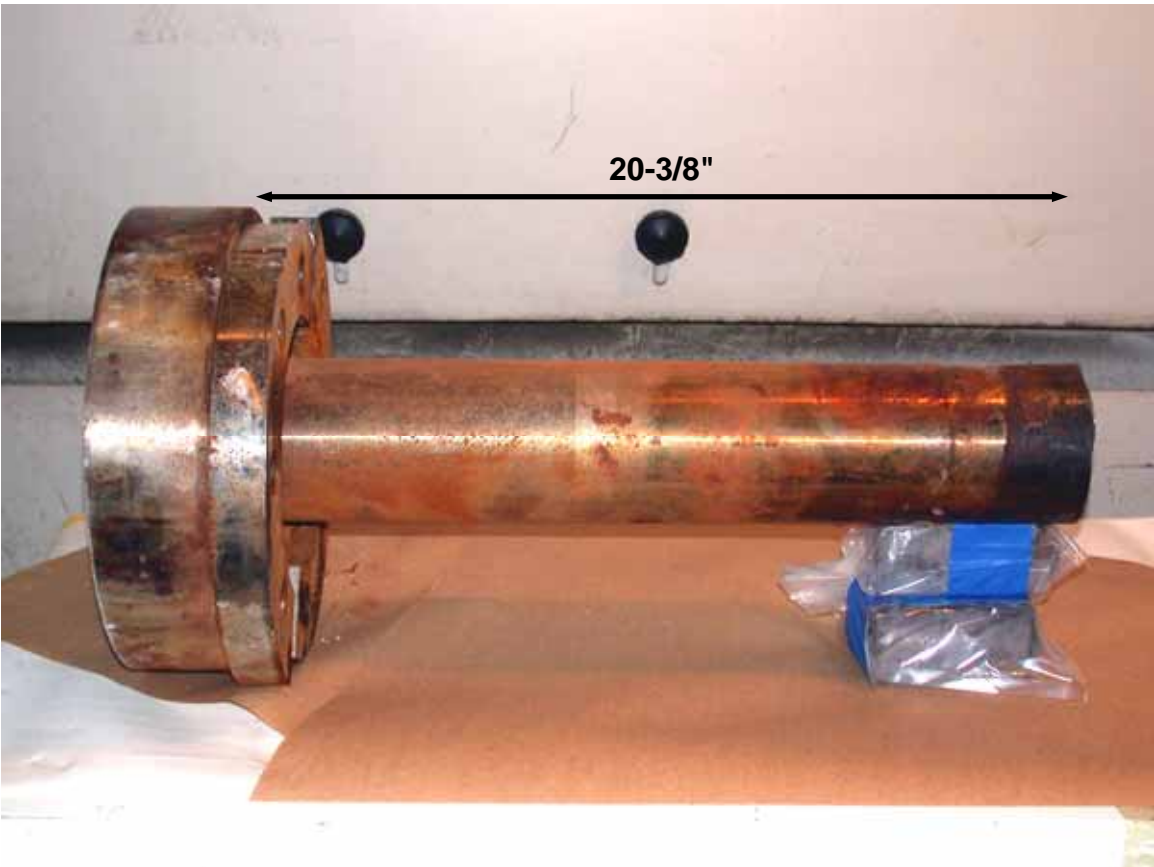


Figure 1.1.2: On-site NDE of nozzle #3 showed 4 axial cracks. Cracks #1 and #3 were through-wall, while cracks #2 and #4 were partially through-wall.



**Figure 2.1.1: Nozzle #2 side view. Approximately 7-5/8" was bored away during the removal process.**



**Figure 2.1.2: Nozzle #2 end view looking at bottom. The boring tool extended ~3" up from the bottom of the nozzle. There was no evidence of cracking found.**

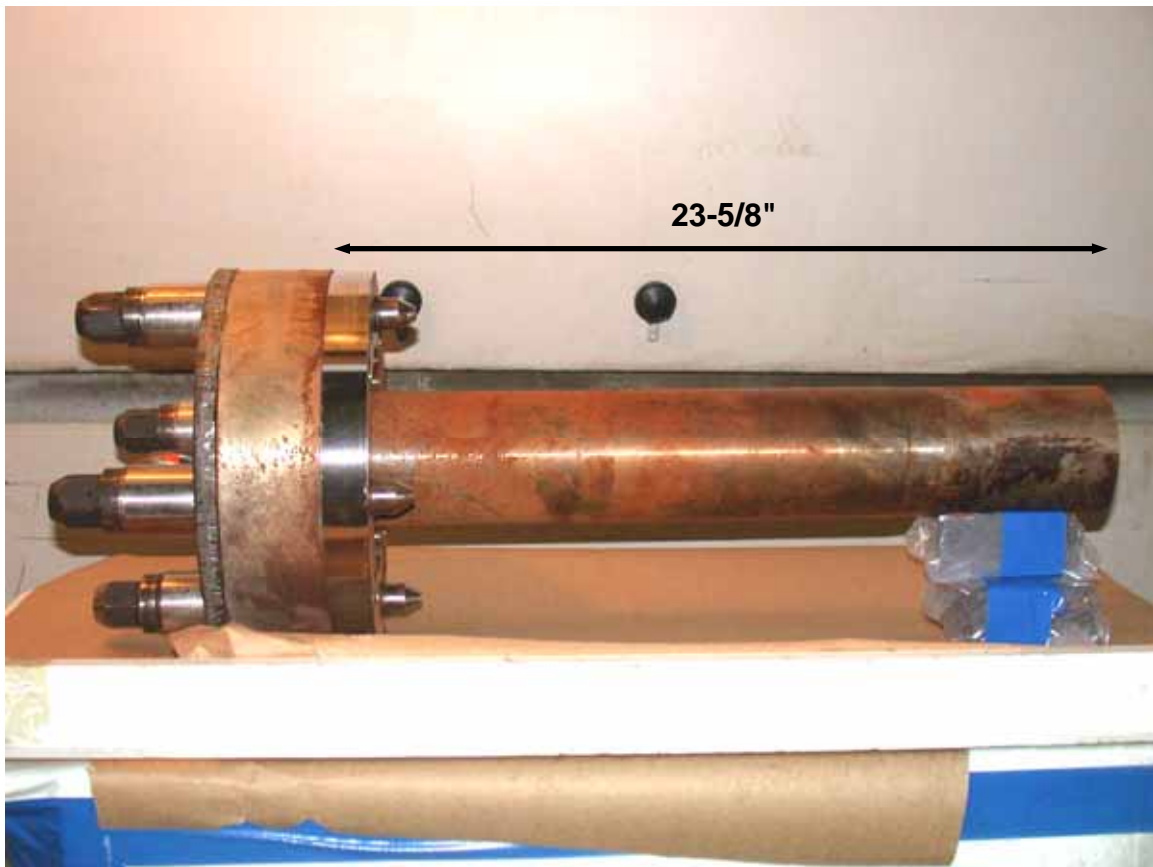


Figure 2.2.1: Nozzle #3 side view. Approximately 4-1/2" was bored away during the removal process. 0° orientation is upward in photo.



Figure 2.2.2a: 0° oriented upward in photo.



Figure 2.2.2b: 90° oriented upward in photo.

Figure 2.2.2: Higher magnification photographs showing end of nozzle #3. Reduced section length was 6-1/2". ~0.5X



Figure 2.2.2c: 180° oriented upward in photo.



Figure 2.2.2d: 270° oriented upward in photo.

Figure 2.2.2 (cont.): Higher magnification photographs showing end of nozzle #3. Reduced section length was 6-1/2". ~0.5X



Figure 2.2.3: Photograph showing end view of nozzle #3.

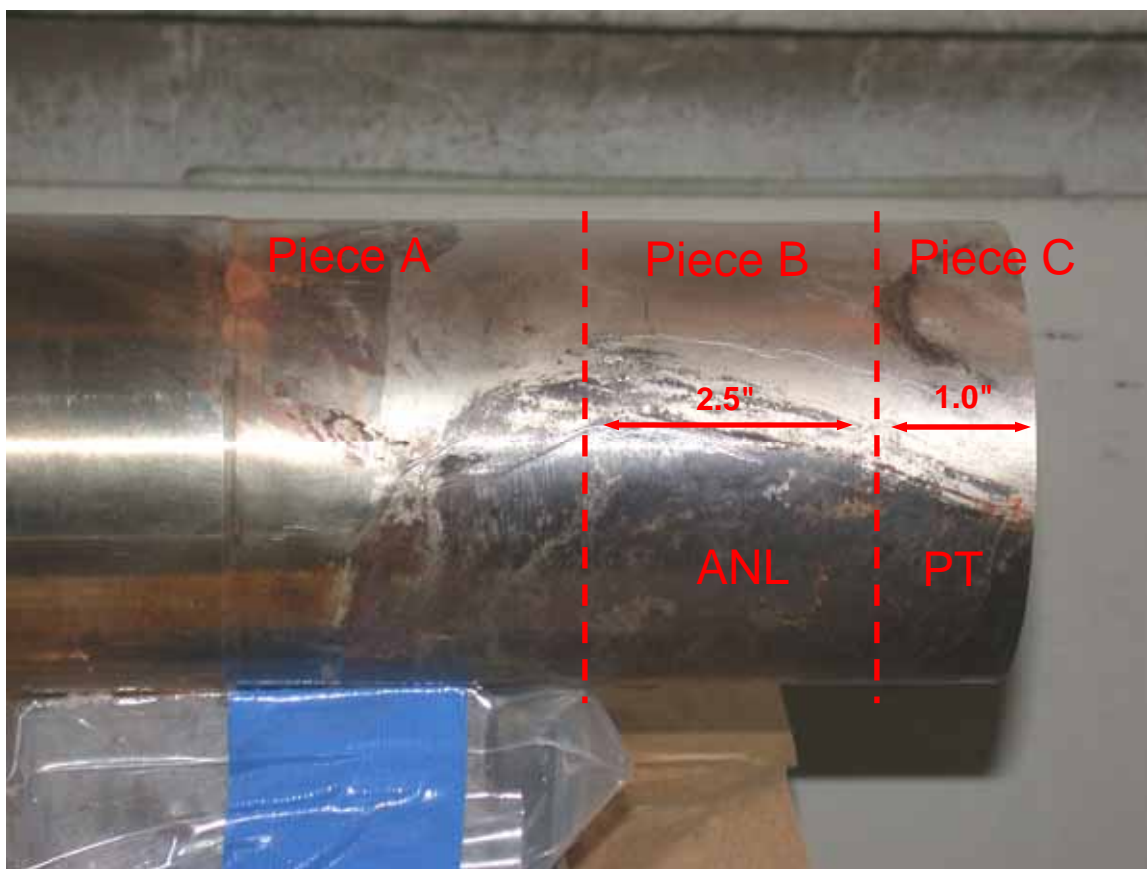
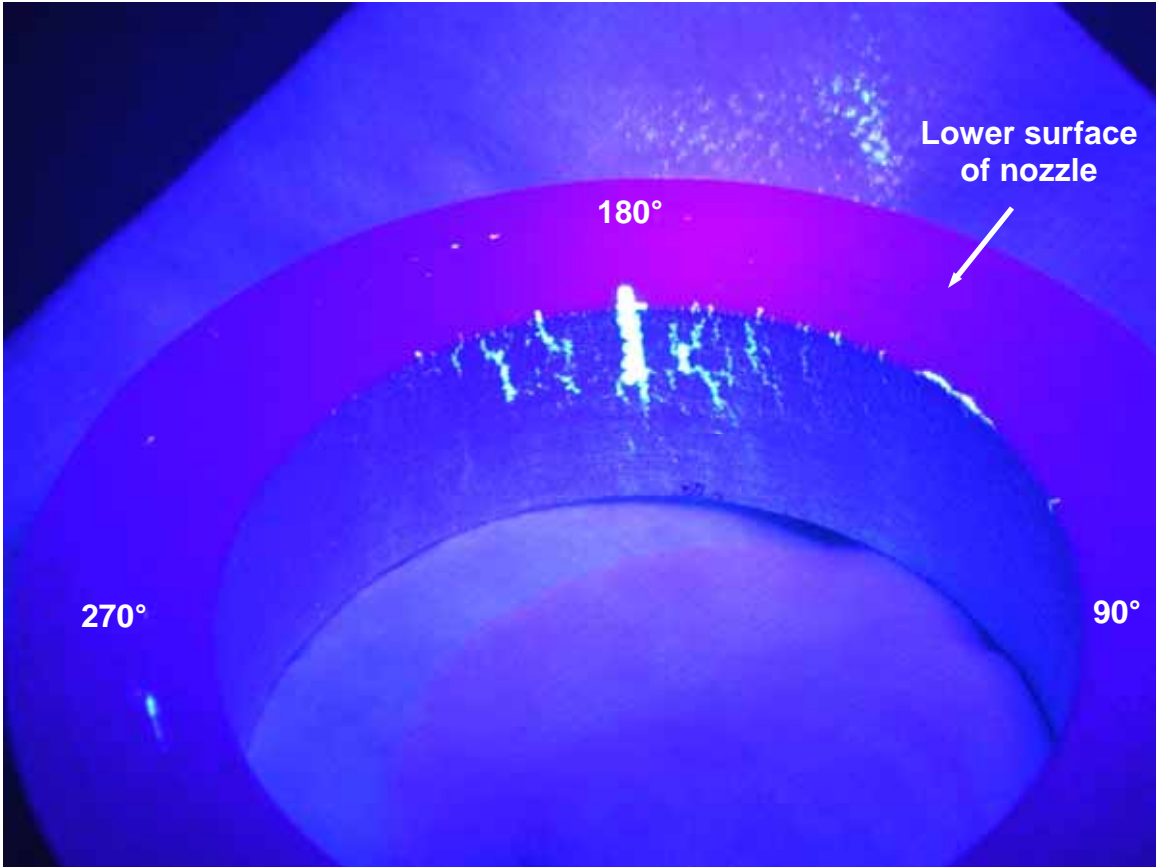
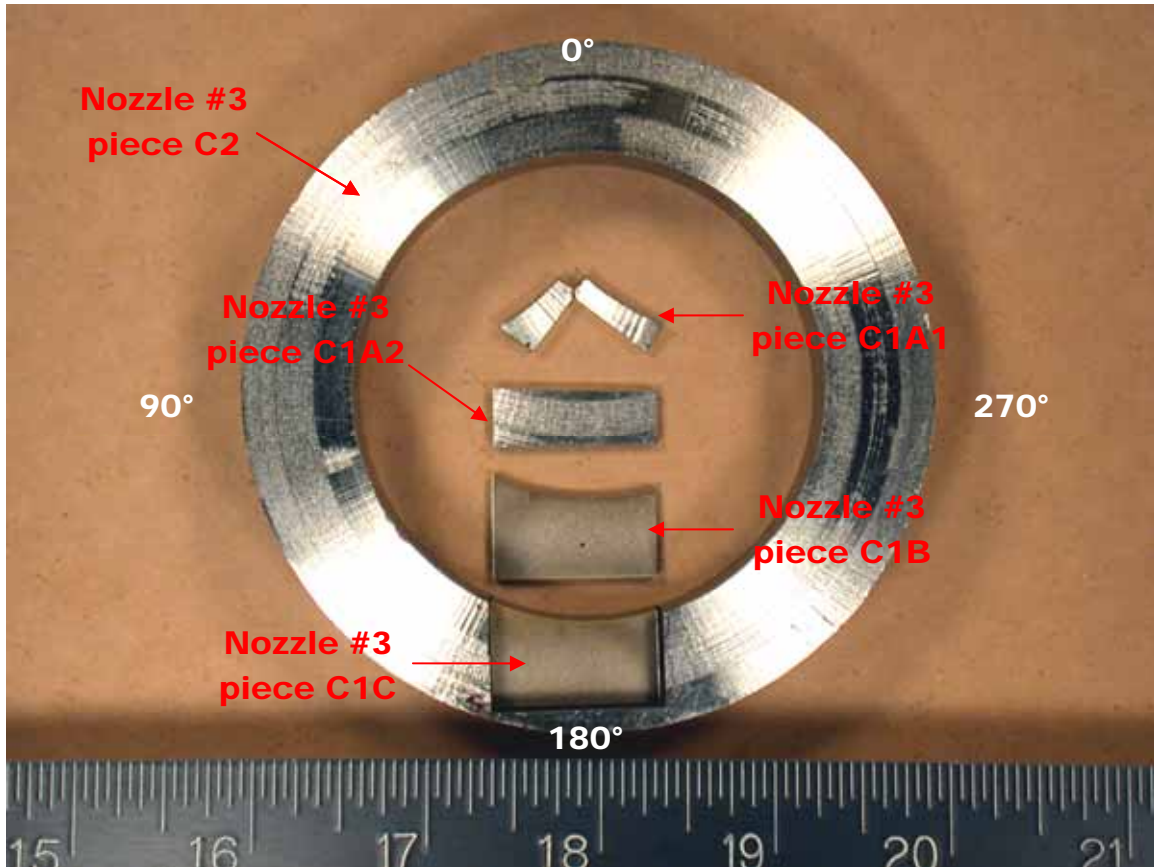


Figure 2.3.1: Sectioning photo for nozzle #3. Piece B was shipped to Argonne National Laboratory and piece C was further tested at BWXT.



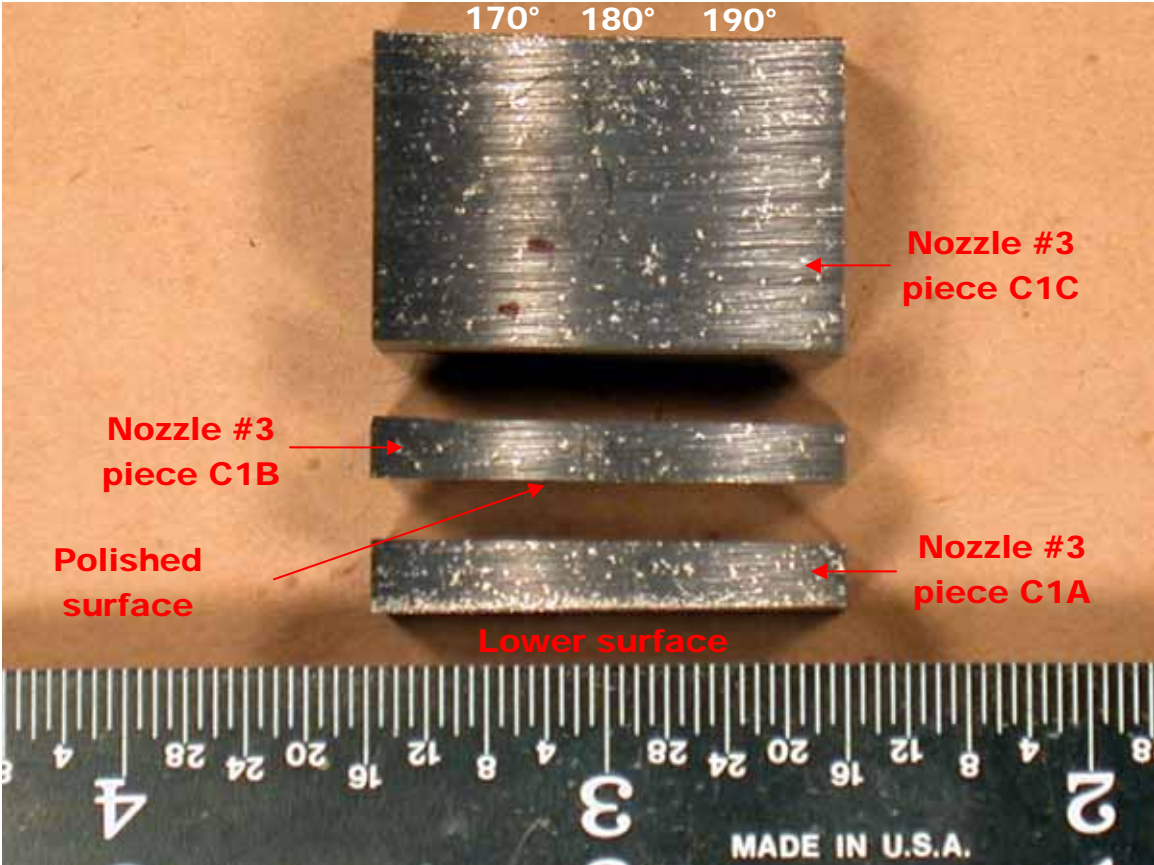
**Figure 2.4.1: Photograph taken under a black light showing the PT results for nozzle #3. Several axial cracks were present near 180°; the largest crack extended ~0.5" in length axially and ~0.125" deep radially from the ID surface.**



Sectioning for nozzle #3 piece C - looking at lower surface

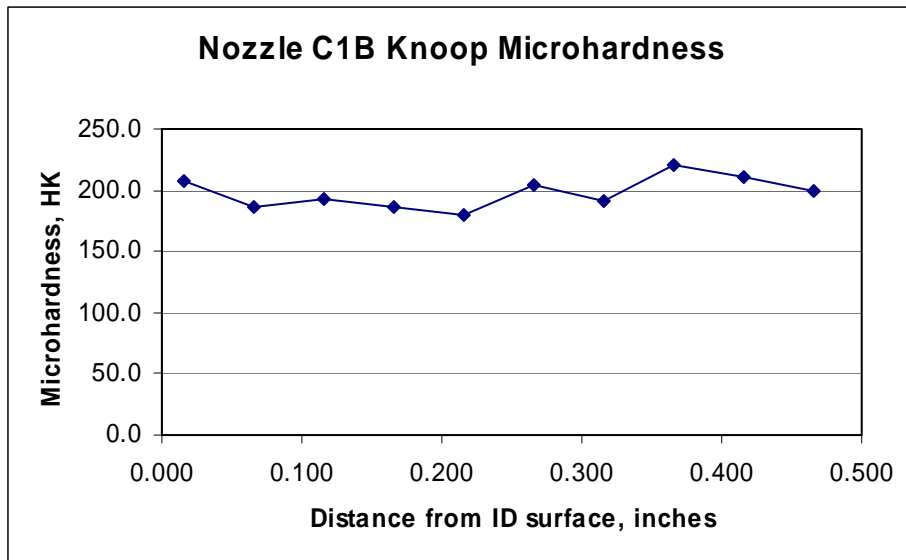
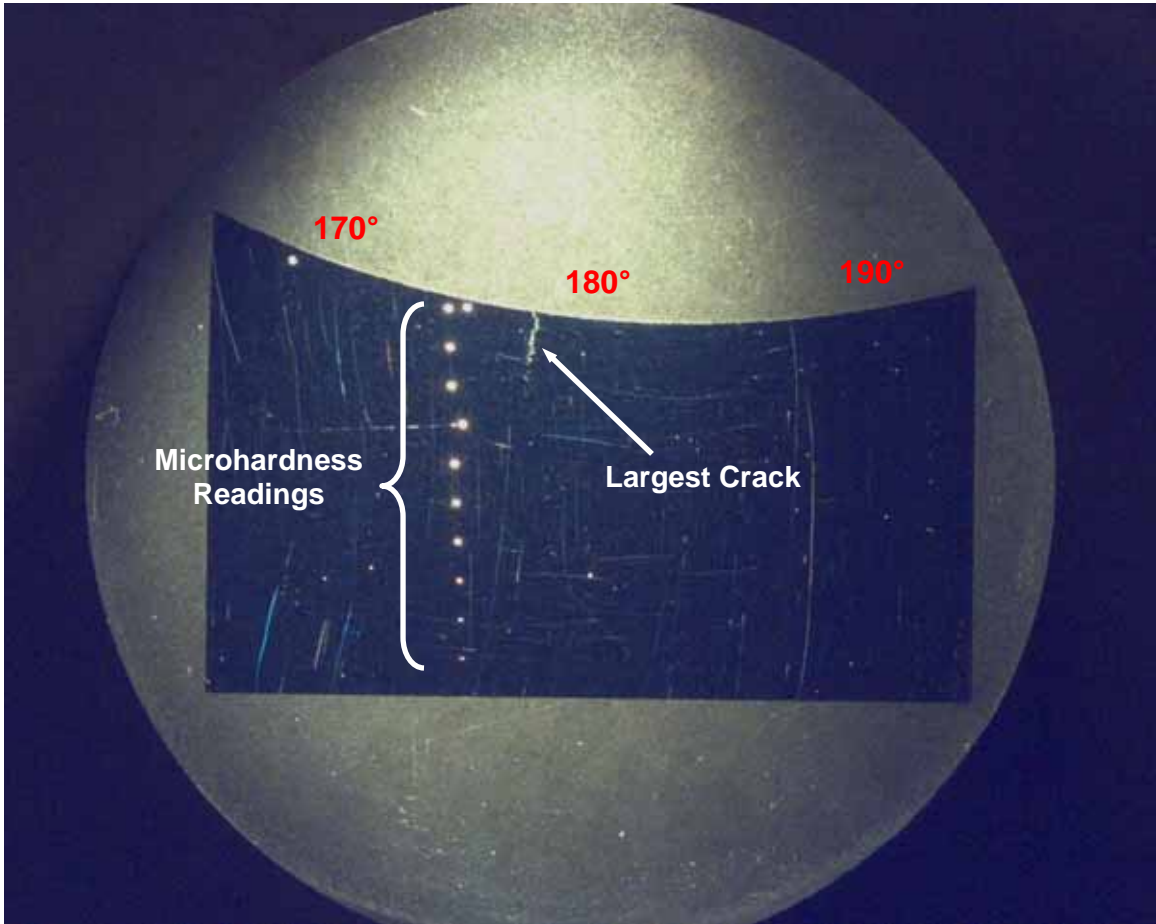
Sample ID	Location	Description	Met	SEM
<b>Nozzle #3 piece C1A1</b>	Lower portion of crack	Open crack sample for SEM/EDS	--	1
Nozzle #3 piece C1A2	Behind lower portion of crack	Spare	--	--
<b>Nozzle #3 piece C1B</b>	Middle portion of crack	Transverse met mount	1	1
<b>Nozzle #3 piece C1C</b>	Upper portion of crack	Reserved for PNL	--	--
Nozzle #3 piece C2	Balance of ring section	Spare	--	--

Figure 2.5.1: Section locations and new sample identifications for nozzle #3 piece C.

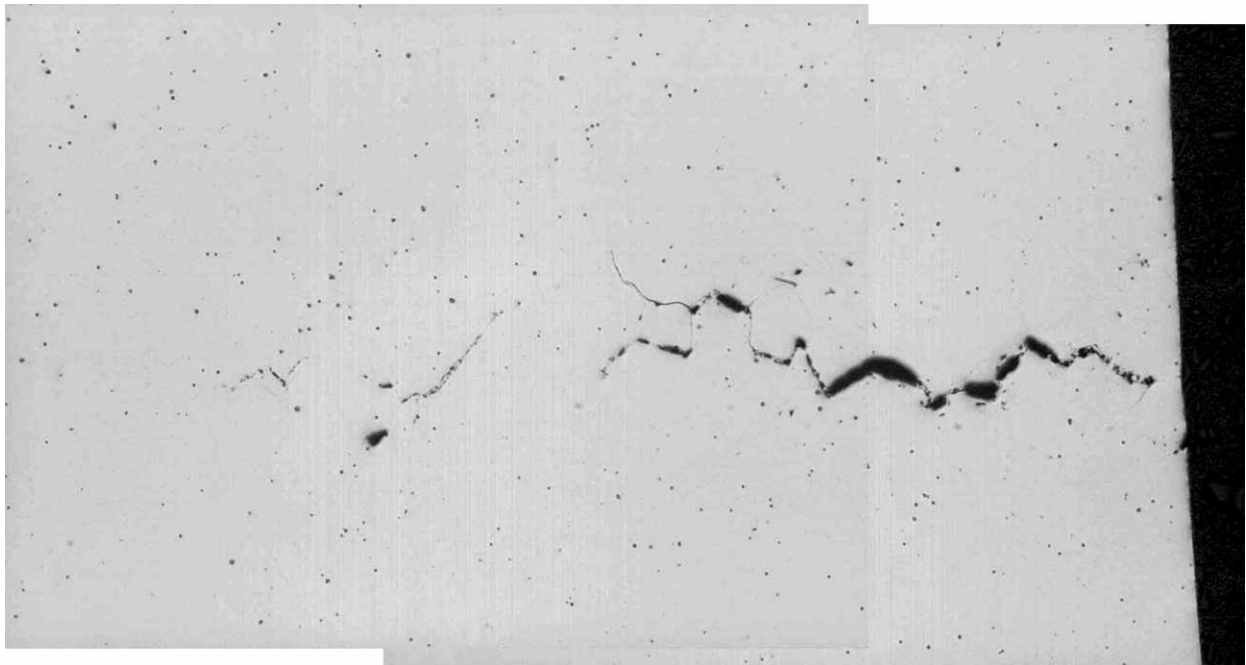


Sectioning for nozzle #3 piece C1 prior to opening lower portion of crack. Looking at nozzle ID surface; the largest crack is located near 180°.

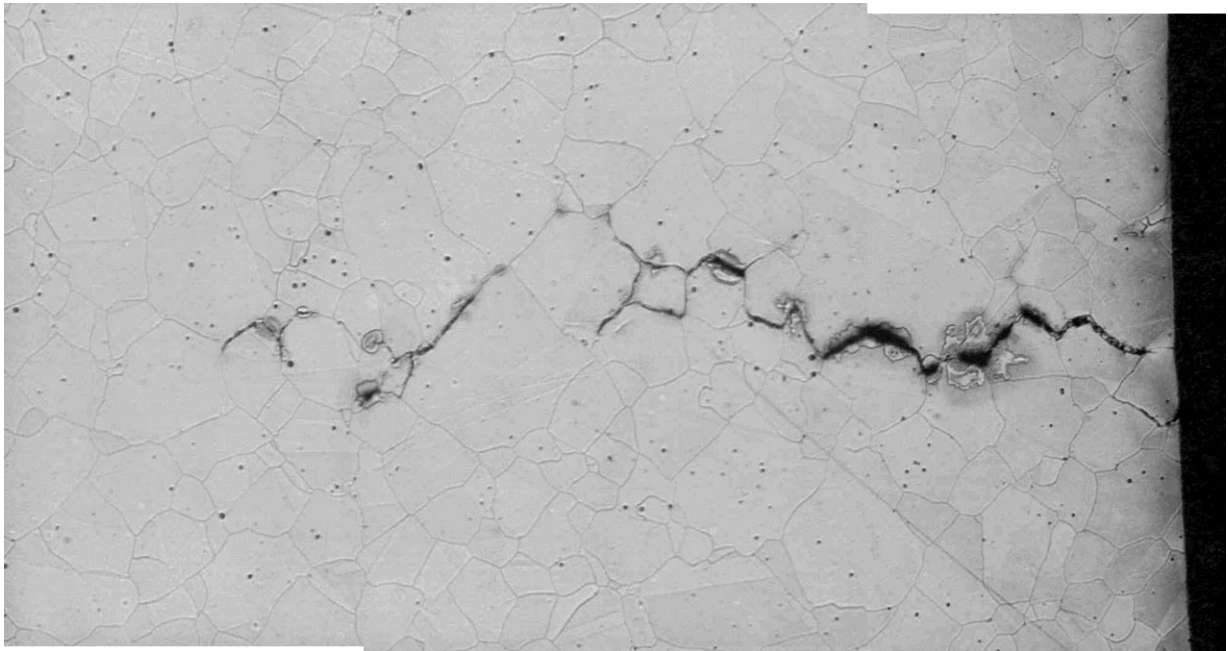
Figure 2.5.2: Photograph of nozzle #3 samples C1A, C1B, and C1C.



**Figure 2.6.1: Low magnification photograph of the nozzle #3 C1B metallographic mount showing location of largest crack and Knoop microhardness indents (top) and microhardness results (bottom).**

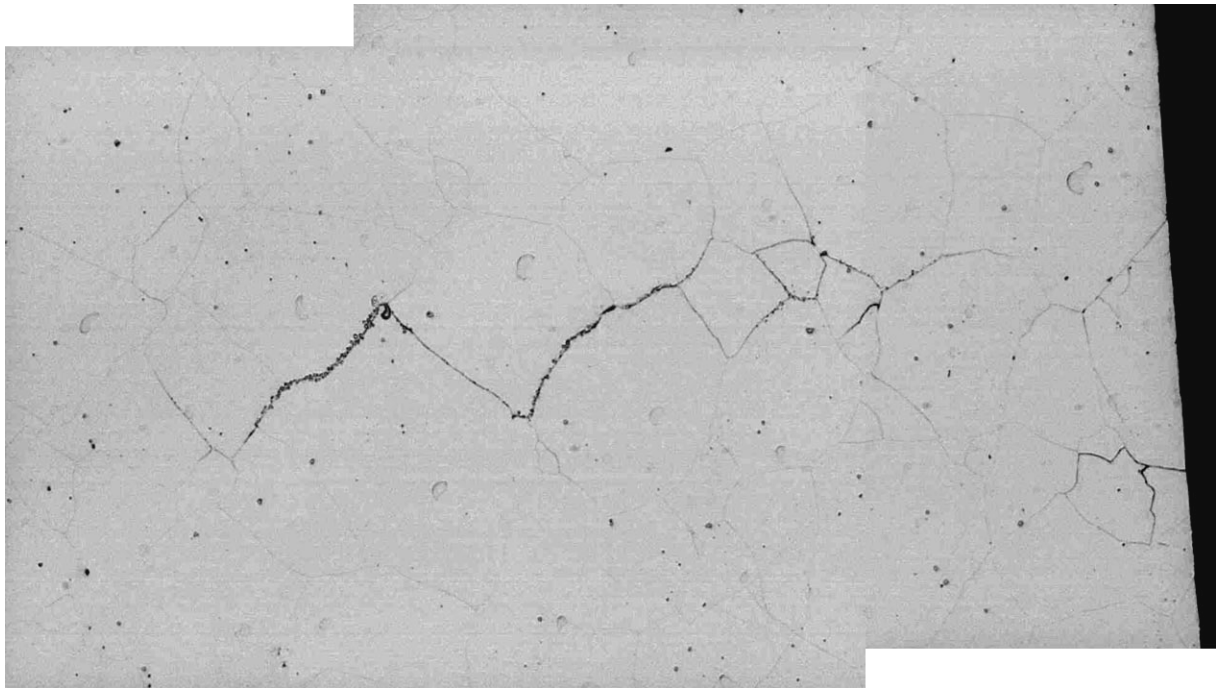


as-polished 48X

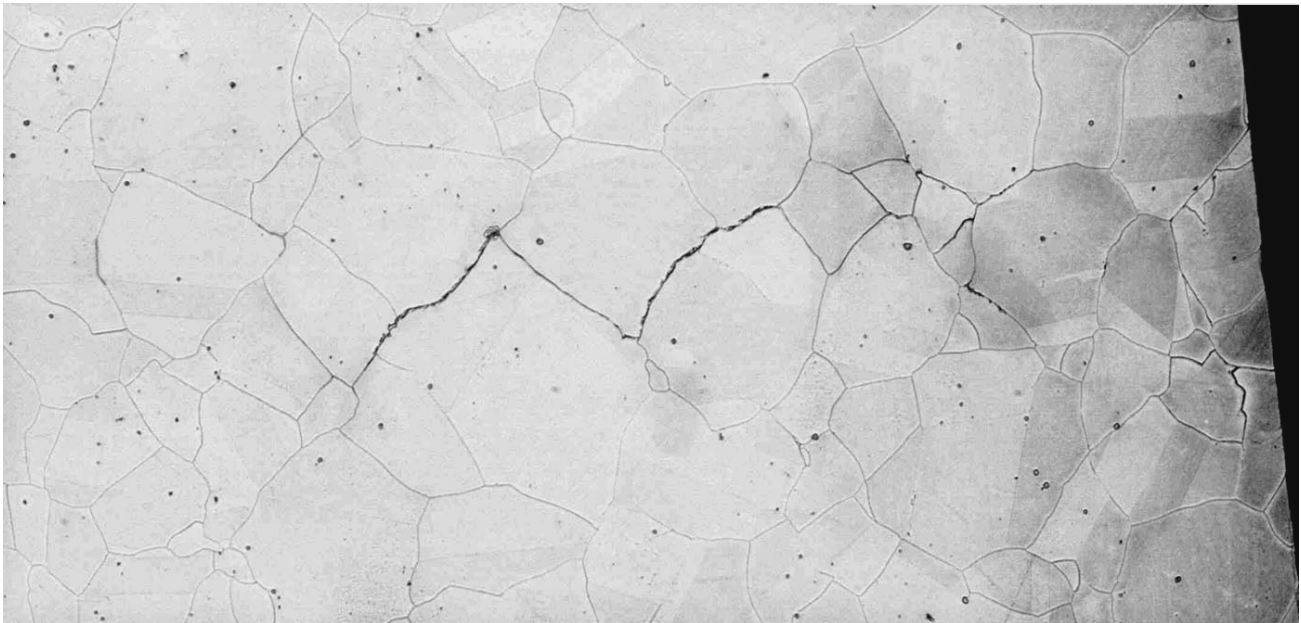


dual etch 48X

**Figure 2.6.2: Micrographs showing the intergranular nature of the largest crack near 180°. The crack extended approximately 0.1" below the nozzle ID surface (located to the right in these micrographs).**



phosphoric etch 100X

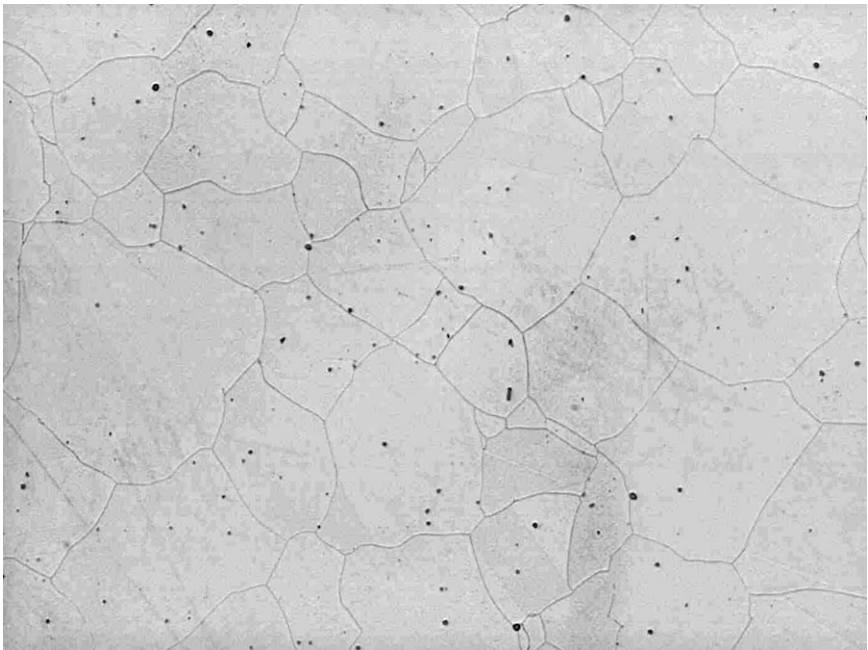


dual etch 100X

**Figure 2.6.3: Micrograph showing the intergranular nature of a smaller nozzle crack located near 170°. This crack penetrated approximately 0.05" below the nozzle ID surface (located to the right in these micrographs).**



phosphoric etch 100X

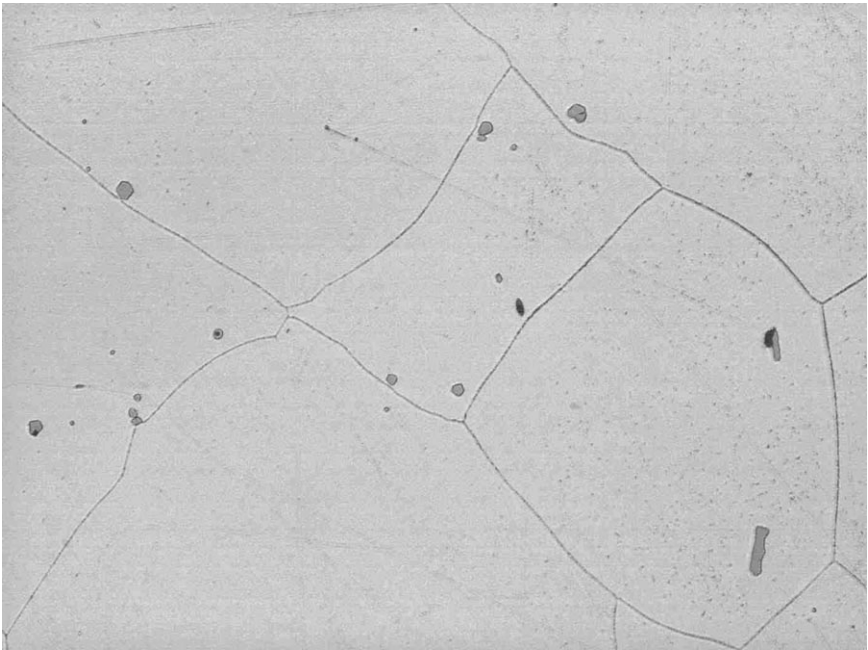


dual etch 100X

**Figure 2.6.4: Typical micrographs of the nozzle base material. The grain size ranged from ASTM 1-6 and averaged ASTM 3.**

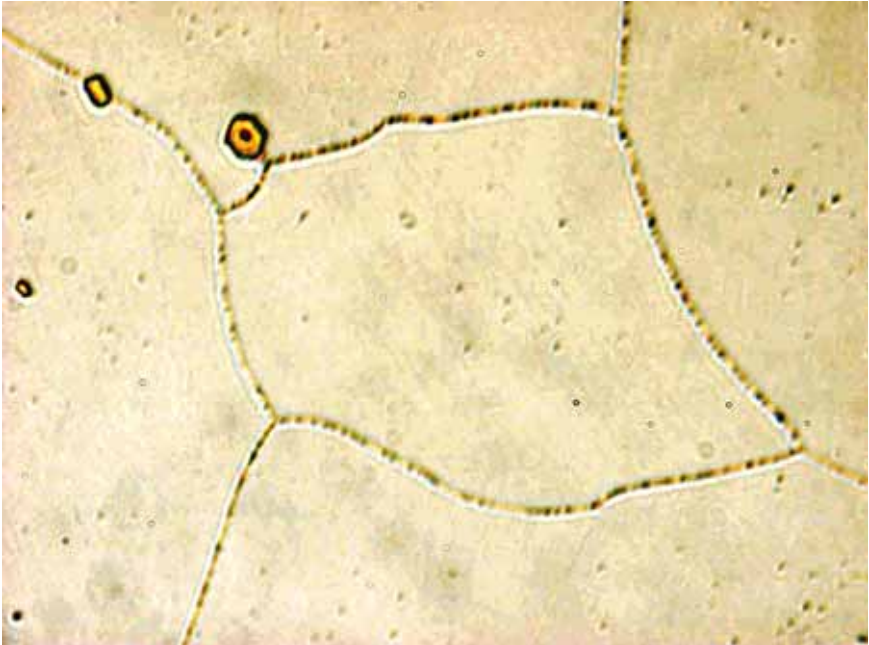


phosphoric etch 375X



dual etch 375X

Figure 2.6.5: Typical micrographs taken of the nozzle base material.



dual etch 960X



dual etch 960X

**Figure 2.6.6: Higher magnification micrographs showing the discontinuous nature of the carbides at the grain boundaries.**

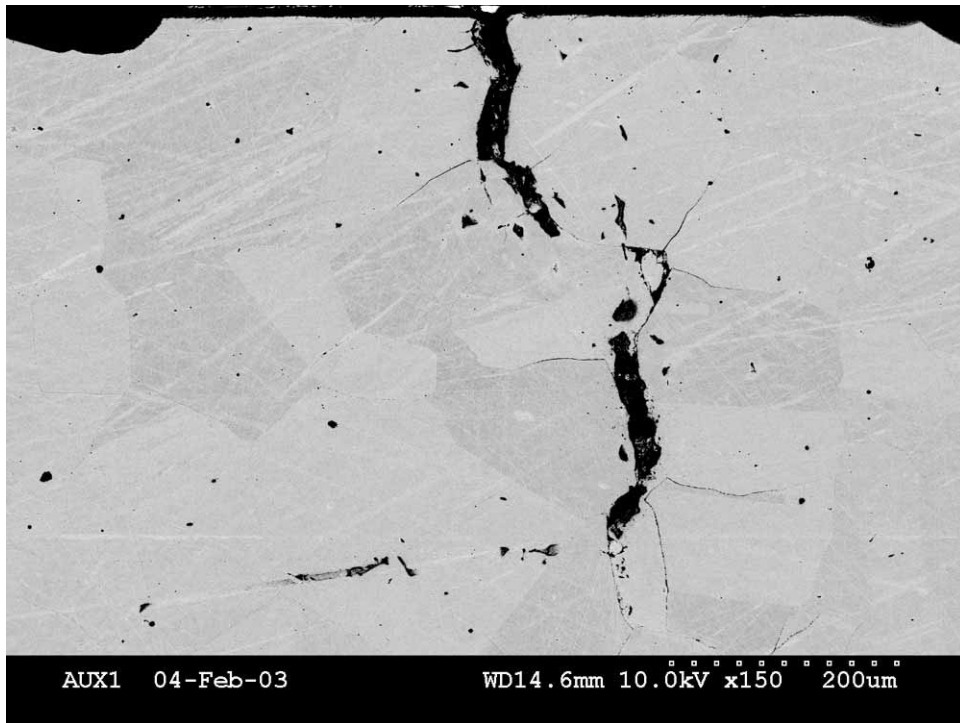
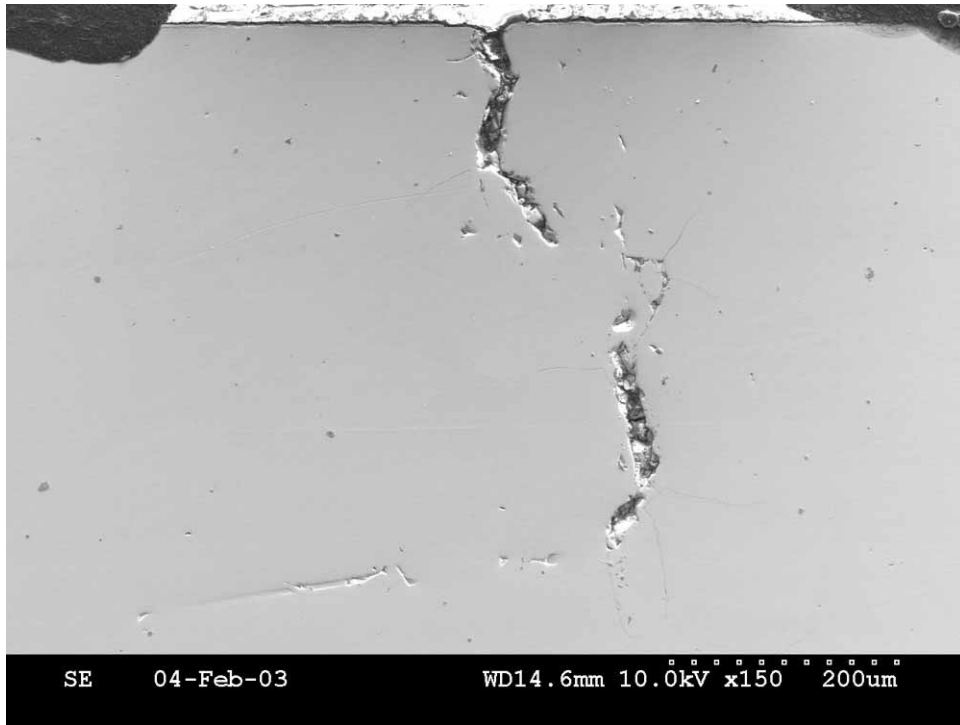


Figure 2.7.1: Low magnification SE (top) and BSE (bottom) taken near the nozzle ID surface (upper edge of micrographs). 150X

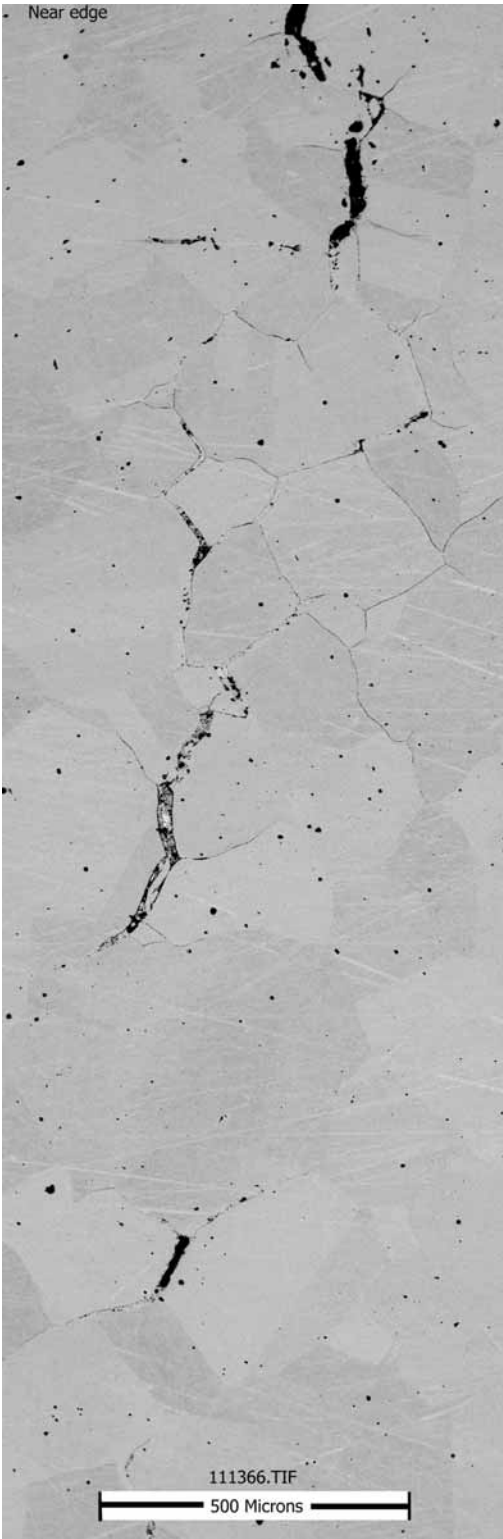


Figure 2.7.2: Mosaic showing full crack length (BSE), which was approximately 0.08" below the ID surface. Cracking was intergranular. ~82X